



Contents lists available at ScienceDirect

Geochimica et Cosmochimica Acta

journal homepage: www.elsevier.com/locate/gca

Episodic ventilation of euxinic bottom waters triggers the formation of black shale-hosted Mn carbonate deposits

Zhi-Guo Dong^{a,b}, Zi-Dong Peng^a, Leslie J. Robbins^c, Kurt O. Konhauser^d, Bang-Lu Zhang^{e,f}, Lian-Chang Zhang^{a,b}, Jie Li^g, Wen-Jun Li^a, Le Zhang^g, Chang-Le Wang^{a,b,*}

^a Key Laboratory of Mineral Resources, Institute of Geology and Geophysics, Chinese Academy of Sciences, Beijing 100029, China

^b University of Chinese Academy of Sciences, Beijing 100049, China

^c Department of Geology, University of Regina, Regina S4S 0A2, Canada

^d Department of Earth and Atmospheric Sciences, University of Alberta, Edmonton T6G 2E3, Canada

^e Development and Research Center, China Geological Survey, Beijing 100037, China

^f China University of Geosciences, Beijing 100083, China

^g State Key Laboratory of Isotope Geochemistry, Guangzhou Institute of Geochemistry, Chinese Academy of Sciences, Guangzhou 510640, China

ARTICLE INFO

Article history:

Received 30 June 2022

Accepted 25 November 2022

Available online 26 November 2022

Associate editor: Eva Stüeken

Keywords:

Ventilation

Euxinic

Formation mechanism

Black shale

Mn carbonate deposit

Ortokarnash

Malkantu

ABSTRACT

Many manganese (Mn) carbonate deposits over geologic history are often closely associated with black shales. However, the mechanism(s) by which the Mn entered the sediments remains controversial because on one hand oxygenated waters are required for primary Mn(IV) oxide formation but on the other hand black shales generally form under reducing conditions. China hosts some of the world's largest black shale-hosted Mn deposits, for example, the Carboniferous Ortokarnash and Malkantu Mn deposits in the Malkansu region, offering a good opportunity to revisit the genesis of black shale-hosted Mn carbonate deposits. Here, we present the first coupled, systematic paleoredox and hydrographic reconstruction of those deposits with the aim of elucidating the redox-state of the depositional basin at the time of their initial deposition. The Mn ore beds in this region are hosted within laminated, organic-rich mudstones (i.e., black shales) reflective of a relatively deep-water depositional environment. The Mn ores are comprised of the Mn(II) carbonate minerals (rhodochrosite and Ca-rhodochrosite), with minor alabandite, pyrite, and monazite. Multiple independent lines of evidence, including positive shale-normalized Ce anomalies (average 3.0), negative $\delta^{13}\text{C}_{\text{VPDB}}$ values (average -11.55‰), and negative $\delta^{98}\text{Mo}_{\text{NIST}+0.25}$ values (average -1.07‰), indicate that the Mn(II) carbonate ores were formed during diagenesis via the coupled oxidation of organic matter and reduction of Mn(IV) oxides originally deposited from an oxygenated water column. However, in apparent contradiction, highly reactive iron to total iron ($\text{Fe}_{\text{HR}}/\text{Fe}_{\text{T}}$; average 0.66) and pyrite iron to highly reactive iron ($\text{Fe}_{\text{Py}}/\text{Fe}_{\text{HR}}$; average 0.71) ratios, combined with a high abundance of small framboidal pyrites (mean diameter $\sim 5\text{ }\mu\text{m}$) with narrow size ranges (standard deviations $< 2\text{ }\mu\text{m}$), suggest that the associated black shales were deposited in euxinic (H_2S -bearing) bottom waters. Euxinia resulted from sluggish water mass circulation, with sedimentary Mo/TOC ratios indicating a relatively strong hydrologic restriction. During this stage, dissolved Mn(II) would have accumulated in euxinic waters but not become permanently fixed into sediments, as indicated by higher degrees of enrichment for Mo over U and lower Mo isotope values than coeval seawater recorded in the black shales. These reveal an active Mn(IV) oxide shuttle across a redox-stratified water column. Combined, the Mn ore intervals document sharp benthic oxygenation of euxinic bottom waters, a process that might be induced by the periodic incursions of oxic seawater associated with eustatic sea level rises. This model is supported by the Mo isotopic characteristics of the Mn carbonate ores, which indicate original Mn oxide precipitation from an overlying water with Mo isotopic composition close to coeval open seawater (minimum $\delta^{98}\text{Mo}_{\text{NIST}+0.25}$ of 1.9‰). In contrast to the generalized “bathtub ring” model envisaging that the black shale-hosted Mn deposits were formed at shallow basin margins, our results

* Corresponding author.

E-mail address: wangcl@mail.iggcas.ac.cn (C.-L. Wang).

highlight that they were more likely formed by *in-situ* ventilation of anoxic (especially euxinic) deep waters of basin center settings. In this regard, we suggest that the ventilation model better explains the close association of Mn carbonate ores with black shales, and has profound implications for understanding the paleoredox framework of otherwise Mn-rich black shale successions.

© 2022 Elsevier Ltd. All rights reserved.

1. Introduction

As a critical industrial metal and an important redox indicator, manganese (Mn) has been a hot research topic in both economic geology and paleoenvironmental studies (Roy, 2006; Maynard, 2010; Beukes et al., 2016; Lyons et al., 2020). The redox cycling of Mn also plays a key role in ocean biogeochemistry because dissolved Mn(II) serves as a crucial micronutrient for marine organisms (Peers and Price, 2004; Browning et al., 2021), while insoluble Mn(IV) (oxyhydr)oxides (hereafter simplified as Mn oxides) can effectively scavenge a variety of bioessential trace metals (e.g., Mo, Cu, Zn, Ni) due to their high adsorptive capacity (Tebo et al., 2004; Hein et al., 2013).

Most Mn enrichments in the sedimentary rock record, especially economic Mn ore deposits, are manifested as reduced Mn (II) carbonate minerals (Maynard, 2010; Johnson et al., 2016). Generally, it is assumed that Mn carbonate ores throughout Earth's history originated from the diagenetic conversion of solid-phase Mn oxides that were initially deposited under oxic water columns (Calvert and Pedersen, 1996; Maynard, 2010; Johnson et al., 2016; Beukes et al., 2016; Yan et al., 2022). Evidence for this diagenetic origin of Mn carbonate ores includes Mn oxide relics enclosed by Mn carbonate minerals (e.g., Johnson et al., 2016; Zhang et al., 2020; Yan et al., 2022), negative inorganic carbon isotope values (e.g., Okita et al., 1988; Tsikos et al., 2003; Huang et al., 2022), and positive shale-normalized cerium anomalies (e.g., Gutzmer and Beukes, 1998; Chisonga et al., 2012; Xiao et al., 2017). Collectively, these lines of evidence indicate that the reduction of original Mn oxides in the sediment pile, coupled to organic matter oxidation, resulted in the generation of the Mn carbonates. By contrast, the direct precipitation of Mn-bearing carbonates from anoxic limnic waters has recently been observed, indicating that the formation of Mn carbonate deposits may not necessarily require the initial burial of Mn oxides, and by inference, oxic bottom waters (Herndon et al., 2018; Wittkop et al., 2020). Nevertheless, the application of molybdenum (Mo) isotopes, whose fractionation in seawater is dominated by Mn oxide adsorption (Barling and Anbar, 2004; Wasylenki et al., 2008), to Mn carbonate deposits (or enrichments) provides compelling support for primary Mn oxide burial (e.g., Planavsky et al., 2014; Goto et al., 2021; Dong et al., 2022).

Based on the host rocks, Mn carbonate ore deposits throughout Earth's history can be broadly grouped as either black shale or limestone-hosted (Fan et al., 1992; Gutzmer and Beukes, 1998), with additional minor deposits hosted by iron formations (Beukes et al., 2016). Arising from this distribution, there is a consensus that sedimentary Mn mineralization is closely related to the water column redox conditions (Frakes and Bolton, 1992; Roy, 2006; Häusler et al., 2018). Given the high solubility of Mn under reducing conditions, anoxic seawater is believed to be essential for the transport and accumulation of dissolved Mn(II) that leads to subsequent mineralization (Force and Cannon, 1988; Polgári et al., 1991). This notion coincides with the temporally widespread occurrences of Mn carbonate deposits – spanning much of the Phanerozoic (Fig. 1) – that are closely associated with organic-rich (TOC greater than 1 wt%), fine-grained siliciclastic sediments (i.e., black shales), which generally indicate the presence of

water-column anoxia (Force and Cannon, 1988; Arthur and Sageman, 1994).

Considering the clearly different redox conditions where primary Mn oxide minerals and associated black shales were deposited, it seems that the black shale-hosted sedimentary Mn carbonate metallogenesis requires a nuanced combination of anoxic and oxic water column conditions. Currently, black shale-hosted Mn carbonate deposits are commonly assumed to be deposited on the margin of a redox-stratified basin (i.e., the so-called “bathtub ring” model), where deeper anoxic seawater replete with dissolved Mn(II) was upwelled to shallower oxic environments, where Mn oxide deposition was triggered (Frakes and Bolton, 1984; Force and Cannon, 1988; Roy, 2006; Maynard, 2010; Zhang et al., 2020). However, the spatial–temporal redox configuration involved in this model is difficult to reconcile with the close association between Mn carbonate ores and black shales, which were generally deposited under anoxic, deeper-water conditions rather than oxic conditions that prevail on shallow basin margins (e.g., Arthur and Sageman, 1994; Beukes et al., 2016). In contrast, modern observations reveal that the Mn mineralization in sapropels of the Baltic Sea deeps is induced by the periodic incursions of Atlantic seawater, resulting in the intermittent oxygenation of euxinic bottom waters and concomitant deposition of primary Mn oxides (e.g., Huckriede and Meischner, 1996; Dellwig et al., 2018). Yu et al. (2016) invoked this ventilation model, analogous to the processes observed in the Baltic Sea, to explain the Datangpo-type Mn deposits based on their paleogeographic distribution in the deep grabens of the Nanhua basin. To date, however, the potential for this ventilation model to be more widely applied to ancient black shale-hosted Mn deposits remains unclear, and has yet to be investigated in detail.

Newly discovered Carboniferous black shale-hosted Mn deposits in the Malkansu region of northwestern China contain high-grade Mn carbonate ores (average Mn greater than 35 wt%), and present a good opportunity to revisit the genesis of black

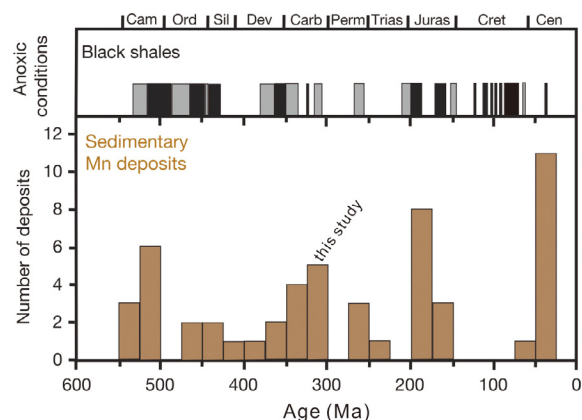


Fig. 1. Secular distribution of Phanerozoic black shales and sedimentary Mn deposits, showing the age of Mn deposits used in this study. Black shale deposition typically indicates anoxic conditions, with black bars signifying global periods of anoxia and gray bars signifying limited periods of anoxia. Adapted from Bekker et al. (2014)

shale-hosted Mn carbonate deposits. Here, geochemical techniques including iron speciation, C–S–Mo isotopes, and trace metal elements, are integrated with petrography and mineralogy. This systematic approach is applied to both the Mn ore layers and immediately underlying and overlying black shales, aiming to obtain a more comprehensive understanding of basin redox and hydrologic variations immediately before, during, and after Mn deposition. Our results reveal that episodic ventilation of euxinic bottom waters in restricted environments triggered the formation of the Malkansu Mn deposits. Consequently, we suggest that the ventilation model is applicable to ancient black shale-hosted Mn carbonate deposits, and has profound implications for understanding the paleoredox framework of other Mn-rich black shale sequences.

2. Geologic background

2.1. Regional geology

The Western Kunlun Orogen, located along the northwestern periphery of the Tibetan Plateau (Fig. 2a), represents a Paleozoic to early Mesozoic accretion zone that is of considerable importance for the reconstruction of paleo-Asia (Mattern and Schneider, 2000; Xiao et al., 2005). This long-lived accretionary orogenesis in the Western Kunlun area was closely associated with the evolution of both the Proto- and Paleo-Tethys Oceans (Xiao et al., 2003; Han et al., 2016). From north to south, the Western Kunlun Orogen can be tectonically divided into the North Kunlun Terrane (NKT), the South Kunlun Terrane (SKT), and the Tianshuihai Terrane (TST), separated by the Kudi and Kangxiwa sutures, respectively (Fig. 2a; Xiao et al., 2005; Zhang et al., 2019). In the early Paleozoic, the Western Kunlun area was an active continental margin with the southward subduction of the Proto-Tethys Ocean beneath the Tianshuihai Terrane (Zhang et al., 2018; Peng et al., 2021b).

Beginning in the late Paleozoic, northward subduction of the Paleo-Tethys Ocean towards the Tarim Craton generated a series of back-arc basins along the North Kunlun Terrane, such as the Malkansu, Oytag, and Tamu basins (Ji et al., 2018; Zhang et al., 2021). Among them, the Malkansu basin is known for significant Carboniferous sedimentary Mn carbonate mineralization.

The Malkansu basin is situated at the junction of the Tarim Craton, the West Kunlun Orogen, and the Pamir Plateau (Fig. 2a). It was developed on a basement comprised of early Paleozoic metamorphic rocks of greenschist to amphibolite facies, and was then filled by Carboniferous to Permian volcano-sedimentary strata (Zhang et al., 2020b). The Lower Carboniferous Wuluat Formation consists mainly of basaltic pillow lavas with interlayers of chert and limestone, a rock assemblage typical of a back-arc basin (Ji et al., 2018; Zhang et al., 2021). Geochemical studies of the Wuluat Formation volcanic rocks provide additional evidence for their formation in an extensional tectonic setting due to back-arc expansion (Yun et al., 2015; Ji et al., 2018). The Mn ore-bearing Upper Carboniferous Kalaatehe Formation is a succession composed of carbonate and fine-grained siliciclastic sedimentary rocks, representing a platform-dominated sedimentary environment (Zhang et al., 2020a; Dong et al., 2020). During the Early Permian, another volcano-sedimentary cycle took place in the Malkansu basin, resulting in the deposition of andesite and limestone. Subsequently, strata in the Malkansu basin underwent two periods of structural deformation, corresponding to the Late Permian basin closure and the Cenozoic collision between India and Asia (Gao et al., 2018).

2.2. Geology of the Malkansu Mn metallogenic zone

Paleogeographically, the Malkansu basin was located at the northern margin of the Paleo-Tethys Ocean during the Late Carboniferous (Fig. 2b; Li et al., 2018; Zhang et al., 2020a). To be speci-

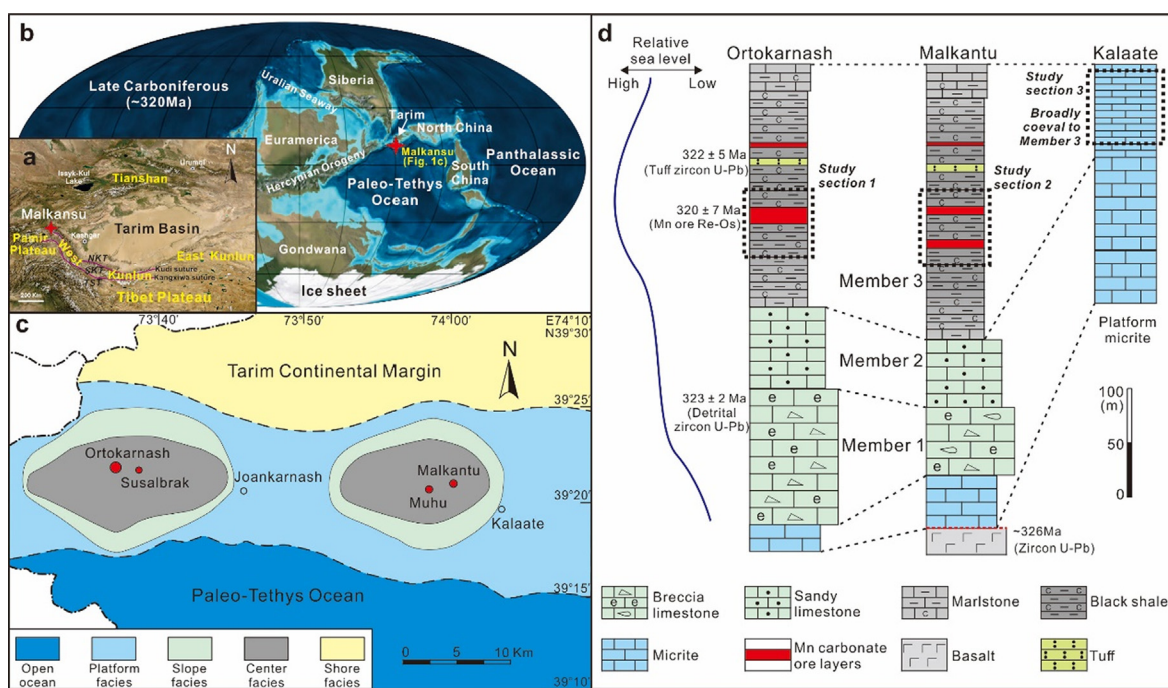


Fig. 2. Locality, paleogeography, and stratigraphy. (a) Schematic tectonic map of Northwest China showing the location of the Malkansu area (red star). NKT, North Kunlun Terrane; SKT, South Kunlun Terrane; TST, Tianshuihai Terrane. (b) Global paleogeographic map of the late Carboniferous (revised from Chen et al., 2018), showing the location of the Malkansu area (red star). (c) Paleogeographic map of the Malkansu basin during deposition of the Kalaatehe Formation, highlighting the spatial distribution of economic Mn deposits (modified from Zhang, 2020). (d) Typical stratigraphic columns of the Kalaatehe Formation in center (Ortokarnash and Malkantu) and platform (Kalaate) facies, respectively. Dashed boxes are selected sections for this study. See the text for references regarding geochronologic dates.

fic, some intra-platform depressions were developed in the Malkansu basin due to continued back-arc rifting, displaying a “platform-depression-platform” paleogeographic framework, as indicated by thinner (~200 m) and thicker (~600 m) sedimentation, respectively (Fig. 2c, d; Zhang, 2020; Zhang et al., 2021). Economic Mn deposits, including the Ortokarnash and Susalbrak deposits in the west, and the Muhu and Malkantu deposits in the east, are distributed in central facies of two major depressions (Fig. 2c). These deposits constitute the well-known giant Malkansu Mn metallogenic zone with total proven Mn ore reserves exceeding 50 million tons (Gao et al., 2018).

The platform-facies Kalaatehe Formation is dominantly composed of thick to thin-bedded (1 m – 0.1 m) micritic limestones, reflecting a relatively shallow-water depositional environment. In contrast, the Mn ore-bearing center-facies Kalaatehe Formation is a succession characterized by carbonate rocks in the lower part and black shales in the upper part. The center-facies succession records the extensional rifting and corresponding tectonic subsidence of the carbonate platform, reflecting continued deepening of the depositional environment. Paleogeographic reconstructions suggest that the black shales should have been approximately contemporaneous with the upper thin-bedded micrites of the adjacent platform-facies succession (Fig. 2d). The Mn ore-bearing succession can be further subdivided into three members (Fig. 2d). From the bottom up, Member 1 is marked by a breccia-bearing limestone in which the breccia is comprised of pyroclasts, bioclasts, and carbonate intraclasts, indicating an unstable depositional environment resulting from the rapid rifting of the platform (Dong et al., 2020). Detrital zircon U–Pb data from the breccia-bearing limestone provide a maximum depositional age of 323 ± 2 Ma (Zhang, 2020). Member 2 is dominated by a sandy limestone composed of sparry calcite and minor quartz and feldspar, reflecting a relatively stable depositional environment and the gradual deepening of the rifted depressions (Zhang et al., 2020a). Member 3 consists mainly of laminated, organic-rich mudstones (i.e., black shales) intercalated with thin-bedded marlstones, Mn carbonate ore layers, and a few tuff beds, suggesting a relatively deep-water depositional environment. Direct Re–Os dating of organic matter within the Mn ores yielded an isochron age of 320 ± 7 Ma (Li et al., 2022), broadly consistent with the zircon U–Pb age of 322 ± 5 Ma for nearby tuff interlayers (Fig. 2d; Zhang, 2020).

This study focuses on the Ortokarnash mine in the west and the Malkantu mine in the east (Fig. 2c). In the Ortokarnash mine there are two Mn ore layers (Fig. 2d) that strike west to east and dip steeply to the north (>70° dip angle). The lower Mn ore layer is the main orebody at the Ortokarnash and extends laterally for more than 5 km, with an average thickness of ~6 m. The upper Mn ore layer at the Ortokarnash mine is laterally discontinuous, and extends ~2.5 km with an average thickness of ~1 m. In the Malkantu mine, there are three Mn ore layers separated by organic-rich black shales (Fig. 2d). Overall, these Mn ore layers are laterally discontinuous, and extend more than 3 km from west to east. The Mn ore layers at the Malkantu dip between 40° and 70° to the south, and have a cumulative thickness averaging ~6 m.

3. Materials and methods

Samples of Mn carbonate ores and associated black shales were systematically collected at an average resolution of 0.8 m to 1 m. At the Ortokarnash mine, samples were collected from a ~12-meter outcrop (GPS coordinates: 73°40'E, 39°20'N), while at the Malkantu mine, samples were collected from a ~17-meter-long drill core (ZK2302; GPS coordinates: 74°02'E, 39°21'N). For comparative study, thin-bedded platform micrites were also sampled from the Kalaate section (GPS coordinates: 74°03'E, 39°22'N) (Fig. 2c and

d). All samples are devoid of evidence for surface oxidation and do not contain macroscopic pyrite nodules and/or quartz-carbonate veins.

3.1. Petrographic and mineralogical investigations

Petrographic and mineralogical observations were made on thin-sections using an optical microscope and a scanning electron microscope (SEM; LEO1450VP). Qualitative chemical compositions of the observed minerals were determined using an energy-dispersive spectrometer (EDS; OXFORD INCA ENERGR 300) attached to the SEM. Moreover, pyrite framboid size distributions were investigated for black shale samples, with the diameters of greater than 1500 framboids measured directly on the SEM. For each sample, at least 100 framboids were measured to obtain a statistically robust size distribution. The above analyses were performed at the Institute of Geology and Geophysics, Chinese Academy of Sciences (IGGCAS).

3.2. Major and trace elements

Samples showing no signs of surface oxidation, veins, or macroscopic pyrite were pulverized into powders (~200 mesh) in an agate mill for bulk chemical and isotopic analyses. Major elements were determined via X-ray fluorescence spectrometry (XRF; AXIOS Minerals), with analytical uncertainties <5 %. Total organic carbon (TOC) contents were measured with a LECO CS-400 infrared carbon–sulfur analyzer. The above analyses were performed at ALS Chemex (Guangzhou, China). Trace element analyses were carried out at Guizhou Tongwei Analytical Technology Co., Ltd. (China). Sample powders were first treated with a mixture of 3 mL HCl (~12 M) + 1 mL HNO₃ (~15 M) + 1 mL HF (~24 M) in Teflon vessels, which were then heated at ~200 °C for two days. After that, the solutions were treated with 0.5 mL 10 M H₂O₂ and were heated at ~60 °C for half an hour to digest residual black materials, likely organic matter with lesser Mn-bearing compounds. This procedure was repeated several times until the residual black materials were totally digested. Trace element concentrations were measured on an inductively coupled plasma-mass spectrometer (ICP-MS; Thermo Fisher X2). Four internal standards (Rh, In, Re, Bi) were used to correct for instrument drift during analysis. Two international geostandards (W-2a and BHVO-2) were used to monitor the analytical quality, yielding precision better than ± 5 %.

3.3. Iron speciation

Iron speciation analyses were conducted on organic-rich black shale samples at the State Key Laboratory of Biogeology and Environmental Geology, China University of Geosciences (Wuhan). Specifically, iron contents in the carbonate (Fe_{carb}), magnetite (Fe_{mag}), and ferric oxide (Fe_{ox}) fractions were sequentially extracted following the procedure of Poulton and Canfield (2005) and measured by atomic absorption spectroscopy (AAS) with the relative standard deviations (RSD) below 5 %. Iron content in pyrite (Fe_{py}) was stoichiometrically calculated based on the content of sulfide (i.e., pyrite) sulfur (S_{sulfide}), which was extracted and precipitated as Ag₂S using the chromium reduction method (Canfield et al., 1986). The chromium reduction method was also used to determine the sulfide (including pyrite and alabandite) sulfur content of the Mn ore samples.

3.4. Sulfur and carbon isotopes

Bulk sulfide sulfur isotope ($\delta^{34}\text{S}_{\text{sulfide}}$) measurements for both Mn ore and black shale samples were made on the extracted Ag₂S precipitates at the State Key Laboratory of Biogeology and

Environmental Geology, China University of Geosciences (Wuhan). Sulfur ratios were measured on a Finnigan MAT 251 mass spectrometer, with results reported relative to the international Vienna Canyon Diablo Troilite (VCDT) standard. Analytical precision is estimated to be better than ± 0.1 ‰, based on replicate analysis ($n = 5$) of IAEA international standards: IAEA S1 (-0.3 ‰), IAEA S2 (22.7 ‰), and IAEA S3 (-32.3 ‰).

Carbonate carbon isotopic compositions ($\delta^{13}\text{C}_{\text{carb}}$) for Mn ore and micrite samples were measured on the whole-rock powders at the IGCAS. The CO_2 extraction for carbonates was accomplished through reaction with anhydrous phosphoric acid, and subsequently the carbon isotope ratios were measured on a MAT-253 mass spectrometer. Results are presented relative to the Vienna Pee Dee Belemnite (VPDB) standard, with analytical error better than ± 0.15 ‰.

3.5. Molybdenum isotopes

Bulk-rock Mo abundances and isotopic compositions of Mn ore and black shale samples were determined using the double-spike method. Complete sample digestion was achieved via the method used in trace element analysis at the Guizhou Tongwei Analytical Technology Co., Ltd. (China), and the subsequent chemical purification of Mo was performed using the ion-exchange chromatography protocol described in Li et al. (2014). Mo isotope ratios were analyzed on a multi-collector inductively coupled plasma-mass spectrometer (MC-ICP-MS; Thermo-Fisher Scientific Neptune Plus) at the Guangzhou Institute of Geochemistry, Chinese Academy of Sciences. Mo isotopic ratios are reported relative to the NIST SRM 3134 standard and were then set to $+0.25$ ‰ for ease of comparison with earlier published data: $\delta^{98}\text{Mo}_{\text{NIST}+0.25} = [({}^{98}\text{Mo}/{}^{95}\text{Mo})_{\text{sample}} / ({}^{98}\text{Mo}/{}^{95}\text{Mo})_{\text{NIST3134}} - 1] \times 1000 + 0.25$ (Nägler et al., 2014). External reproducibility of the NIST SRM 3134 standard was better than ± 0.06 ‰ (2SD, $n = 50$). The geochemical reference materials NOD-A-1 (Mn nodule), IAPSO (seawater), and SGR-1b (shale) were analyzed alongside samples to monitor accuracy, yielding $\delta^{98}\text{Mo}_{\text{NIST}+0.25}$ values of -0.76 ± 0.05 ‰ (2SD, $n = 2$), 2.30 ± 0.06 ‰ (2SD, $n = 4$), and 0.36 ± 0.05 ‰ (2SE, $n = 1$), respectively. These results are in excellent agreement with previously reported values (e.g., Zhao et al. 2016; Gaspers et al., 2020).

4. Results

4.1. Petrography and mineralogy

4.1.1. Mn carbonate ore

Manganese ore samples are generally massive and homogeneous (Fig. 3a) or alternatively, occasionally laminated (Fig. 3b). Manganese carbonate minerals, e.g., rhodochrosite (MnCO_3) and Ca-rhodochrosite, are present as cryptocrystalline to microcrystalline aggregates (Fig. 3c–h) and are the dominant mineral phases in the Mn ore samples. Minor organic matter flakes are dispersed throughout the Mn carbonate aggregates (Fig. 3c). Sulfide minerals in the Mn ore samples are sparse, but when present are dominantly alabandite (MnS) intergrown with rhodochrosite (Fig. 3c). In places, pyrite (Fig. 3d) and (Co, Ni)-rich sulfide (Fig. 3e) have also been observed as subhedral to euhedral grains. Note that a few irregular cerium-rich monazite [$(\text{Ce}, \text{La})\text{PO}_4$] grains were observed intergrown with Mn carbonate minerals (Fig. 3f–h). In addition, there is some fibrous Mn-rich chlorite floating on (Fig. 3c) or embedded between Mn carbonate aggregates (Fig. 3g).

4.1.2. Black shale

The black shales that host the Mn ore layers are well laminated, black siliceous mudstone with intercalations of gray calcareous

mudstone (Fig. 4a). The black siliceous mudstone laminae are organic-rich and consist dominantly of fine-grained siliciclastic materials (e.g., quartz, feldspar, and clay minerals), as well as pyrite with minor carbonate minerals. Conversely, the gray calcareous mudstone laminae are relatively organic-poor and contain more carbonate minerals (up to ~ 50 % by volume) (Fig. 4b). In places, chalcedony laminae composed of cryptocrystalline to microcrystalline quartz aggregates alternate with mudstone laminae (Fig. 4c, d). Pyrite in the black shales mostly occurs as framboids (Fig. 4e–i) and, in some instances, as subhedral grains (Fig. 4c). The space between framboid microcrystals is generally infilled (Fig. 4e), while less frequently normal framboids with recognizable boundaries between microcrystals (Fig. 4f) and framboids showing secondary overgrowth (Fig. 4g) are also observed. Overall, pyrite framboids from both the Ortokarnash and Malkantu black shales are small (Fig. 4h, i), with diameter measurements of more than 1500 framboids from 9 samples (4 from Ortokarnash and 5 from Malkantu) revealing mean sizes ranging between 4.62 and 6.02 μm (Fig. 5a; Table S1). Further, pyrite framboid populations from the Ortokarnash and Malkantu black shales have standard deviations clustering around 1.5 μm and skewness varying between 0.44 and 1.98 (Fig. 5a; Table S1).

4.1.3. Micrite

The platform-facies micrite is grayish in color and thin-bedded (5–10 cm thick for single bed). The micrite is composed almost entirely of cryptocrystalline to microcrystalline calcite aggregates with minor sparry calcite (Fig. 4j). Pyrite, bioclastic fragments, and terrigenous detrital minerals are rare in the platform-facies micrite.

4.2. Geochemical and isotopic characteristics

Key geochemical and isotopic results obtained in this study are provided in Table 1 (see Table S2 for full dataset). Fig. 6 shows that both the Ortokarnash and Malkantu sections display similar overall chemostratigraphic trends across the black shale and Mn ore intervals.

4.2.1. Major elements

The black shale intervals are characterized by low Mn contents (average of 0.8 wt%) but higher total iron (Fe_T) contents (average of 2.8 wt%). By contrast, the Mn ore intervals are characterized by distinctive Mn enrichments (average of 35.5 wt%) and low Fe_T contents (average of 0.9 wt%) (Fig. 6a, b). Correspondingly, the Mn ore intervals yield thousand fold higher Mn/Fe ratios than those of the associated black shale intervals (Fig. 6c). In terms of Si and Al, the black shale intervals average 22.3 wt% and 4.9 wt%, respectively; while the Mn ore intervals have much lower Si and Al contents averaging 4.2 wt% and 0.8 wt%, respectively. The TOC and S_{sulfide} contents in the black shale intervals are high and variable, ranging from 0.6 to 4.9 wt% (average 1.6 wt%) and from 0.5 to 3.4 wt% (average 1.5 wt%), respectively; while the Mn ore intervals yield lower TOC and S_{sulfide} contents, varying from 0.3 to 0.9 wt% (average 0.5 wt%) and from 0.01 to 1.6 wt% (average 0.4 wt%), respectively (Fig. 6d, e). Additionally, the major element composition of the micrite samples is dominated by Ca (average of 39.0 wt%) with minor Mg (average of 0.3 wt%). The contents of Fe, Mn, Si, and Al in the micrite samples are each below 0.1 wt%.

4.2.2. Trace metal elements

Trace metal elements are more enriched in the black shale and Mn ore intervals than in the micrite samples. For instance, Co, Ni, Mo, and U in the black shale and Mn ore intervals have average concentrations of 20.28, 51.98, 13.04, and 2.32 ppm and 8.90, 19.10, 7.58, and 2.80 ppm, respectively. The same trace metals in

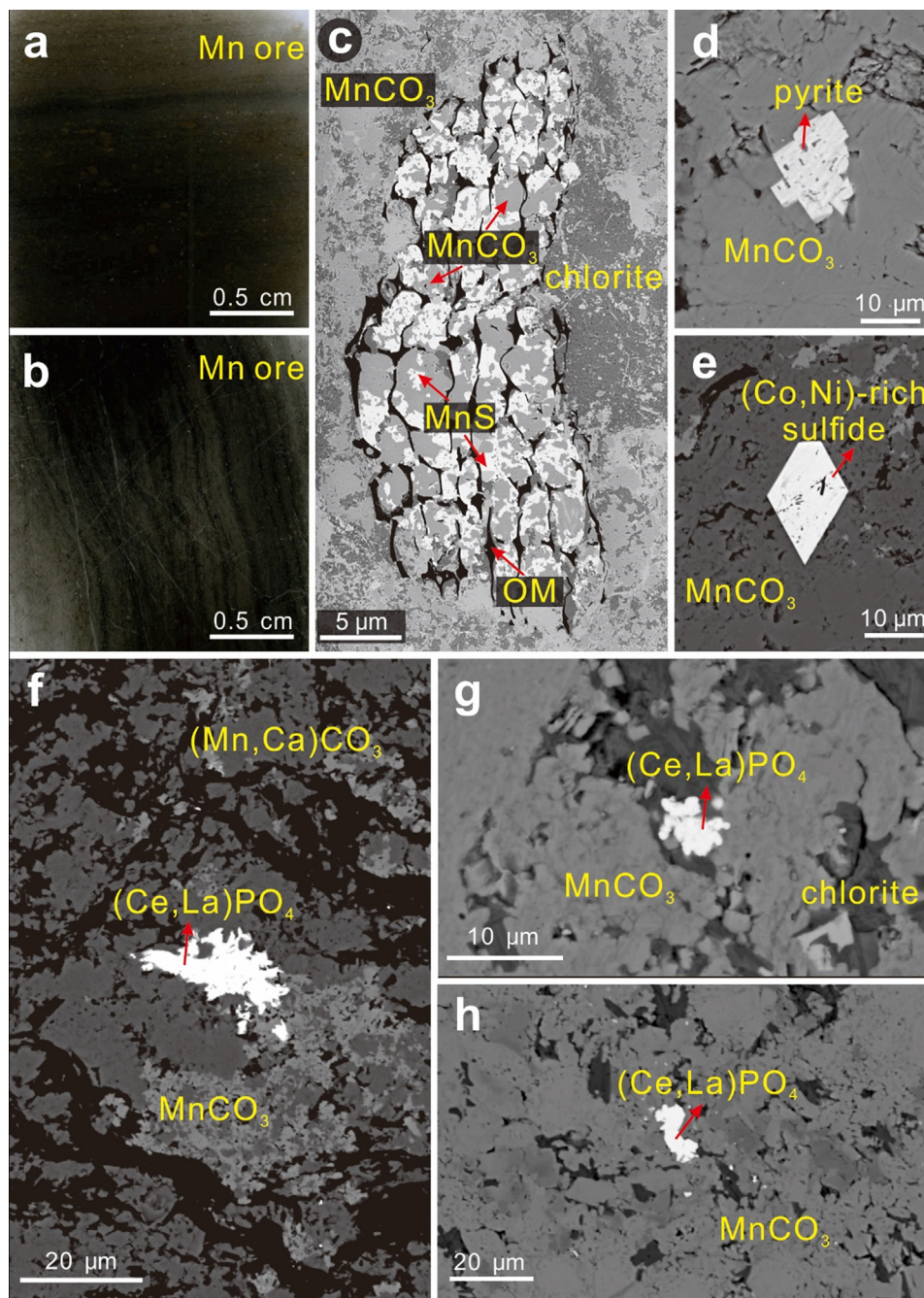


Fig. 3. Petrographic and mineralogical characteristics of the Mn ores. (a–b) Thin section photographs displaying massive (a) and laminated structures (b), respectively. (c) Backscattered electron image (BSE) showing the dispersed organic matter (OM) flakes, as well as the intergrowth of alabandite (MnS) with Mn carbonate aggregates. (d–e) The sporadic subhedral-euhedral pyrite (d) and (Co, Ni)-rich sulfide (e) grains embedded within Mn carbonate minerals (BSE). (f–h) Anhedronal cerium-rich monazite intergrown with Mn carbonate aggregates (BSE).

the micrite samples have relatively lower concentrations, averaging 1.05, 12.56, 0.15, and 3.63 ppm, respectively. Enrichment factors (EF) are commonly utilized to evaluate the degree of authigenic enrichment for trace metals in sedimentary rocks, and can be calculated following the equation of Tribouillard et al. (2006): $X_{EF} = (X/Al)_{sample} / (X/Al)_{PAAS}$, where X represents a given trace metal, and PAAS is the Post-Archean Average Australian Shale composition of Taylor and McLennan (1985). Both the black shale and Mn ore intervals display a certain degree of authigenic enrichment relative to the average shale (i.e., EF greater than 1) with respect to the trace metals mentioned above. Further, some manganese-philic trace metals (e.g., Co, Ni, and Mo; Goto et al., 2021) in

the Mn ore intervals (average Co_{EF} : 5.5; Ni_{EF} : 4.0; Mo_{EF} : 92) have significantly higher enrichment factors relative to those in the black shale intervals (average Co_{EF} : 1.9; Ni_{EF} : 1.7; Mo_{EF} : 24) (Fig. 6g).

4.2.3. Rare earth elements (REE)

The cerium (Ce) and yttrium (Y) anomalies are calculated as follows: $Ce/Ce^*_{PAAS} = [2Ce/(La + Pr)]_{PAAS}$; $Y/Y^*_{PAAS} = [2Y/(Dy + Ho)]_{PAAS}$ (Shields and Stille, 2001; Bau et al., 2014). The Mn ore samples exhibit PAAS-normalized REE patterns characterized by a slight enrichment of the middle REE ($La/Sm_{PAAS} = 0.5–0.8$, mean = 0.7; $Sm/Yb_{PAAS} = 0.8–1.3$, mean = 1.1), highly positive Ce anomalies

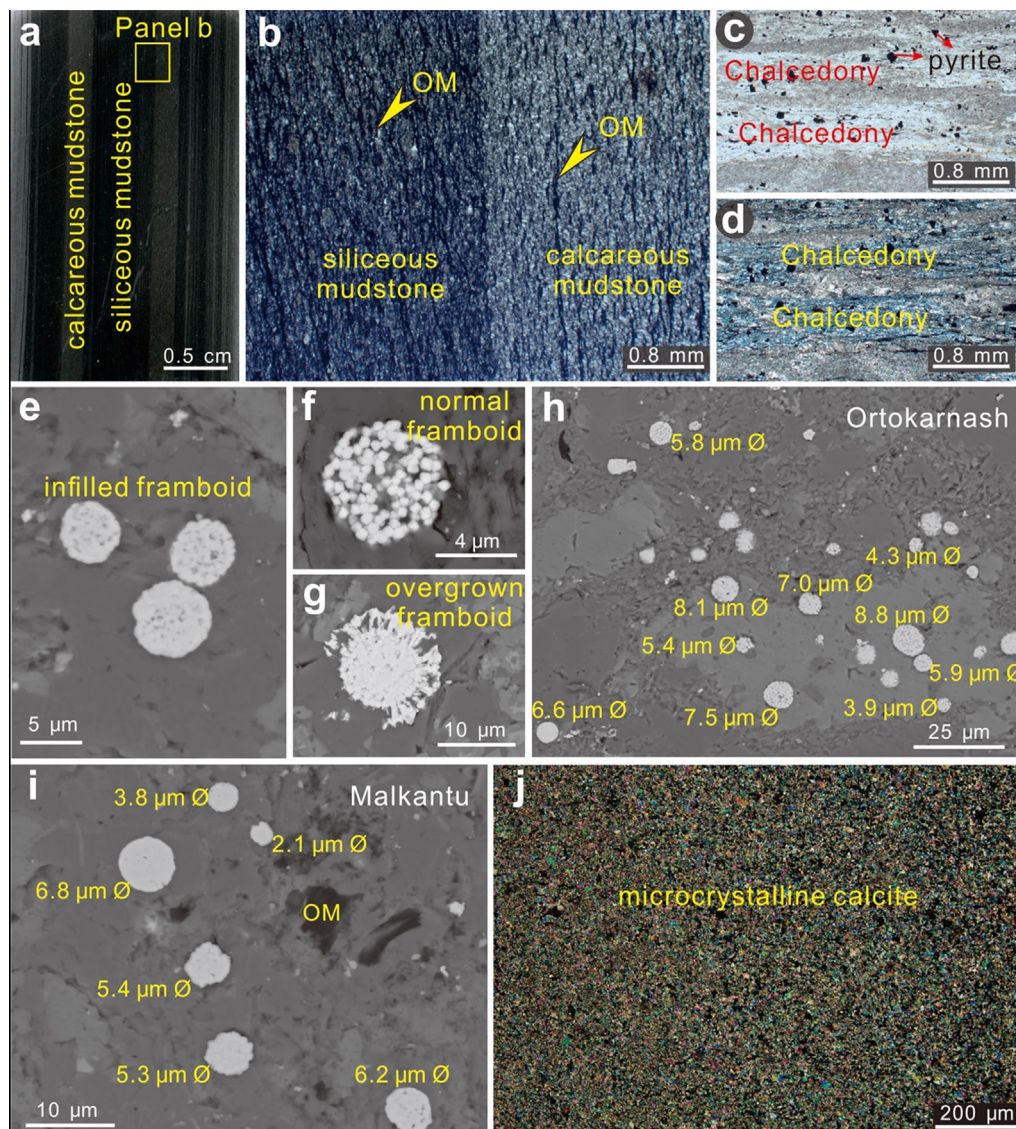


Fig. 4. Petrographic and mineralogical characteristics of associated black shales (a–i) and platform-facies micrite (j). (a) Thin section photograph of black shales showing laminated structure composed of siliceous mudstone with subordinate calcareous mudstone. (b) Close-up of panel a showing OM-rich siliceous mudstone lamina and OM-poor calcareous mudstone lamina (cross-polarized light). (c–d) Chalcedony laminae composed of cryptocrystalline to microcrystalline quartz alternating with mudstone laminae (c under plane-polarized light, d under cross-polarized light). Also note the disseminated subhedral pyrite. (e–i) The abundant framboidal pyrite in black shales (BSE), which can be subdivided into infilled (e), normal (f), and overgrown framboids (g). Framboids from both Ortokanash (h) and Malkantu (i) black shales show small sizes with limited deviation. (j) Platform-facies micrite composed of cryptocrystalline to microcrystalline calcite aggregates (cross-polarized light).

(1.2–3.8; mean = 3.0), and slightly negative Y anomalies (0.8–1.3; mean = 0.9) (Fig. 7). Moreover, the Mn ore samples have lower Y/Ho ratios (22–35; mean = 25) relative to modern seawater (~44; Nozaki et al., 1997). By contrast, PAAS-normalized patterns of the platform micrite samples are slightly depleted in the light REE ($\text{Pr}/\text{Yb}_{\text{PAAS}} = 0.5\text{--}0.7$, mean = 0.5), display pronounced negative Ce anomalies (0.1–0.2; mean = 0.2), and have positive Y anomalies (1.4–1.8; mean = 1.6) (Fig. 7). Further, the micrite samples have Y/Ho ratios (37–47; mean = 42) close to that of modern seawater. Additionally, black shale samples have PAAS-normalized patterns that show a slight depletion in light REE ($\text{Pr}/\text{Yb}_{\text{PAAS}} = 0.2\text{--}0.8$, mean = 0.4) and lack notable Ce anomalies (0.8–1.2, mean = 1.0).

4.2.4. Iron speciation

All black shale samples yield highly reactive iron (including Fe_{carb} , Fe_{mag} , Fe_{ox} , and Fe_{py}) to total iron ratios ($\text{Fe}_{\text{HR}}/\text{Fe}_{\text{T}}$) above 0.22 (Fig. 6i), varying between 0.31 and 1 with an average of

0.66. Furthermore, Fe_{py} dominates Fe_{HR} pools with $\text{Fe}_{\text{py}}/\text{Fe}_{\text{HR}}$ ratios ranging from 0.43 to 0.87, with an average of 0.71. It should be noted that black shales with high $\text{Fe}_{\text{py}}/\text{Fe}_{\text{HR}}$ ratios (greater than 0.7) generally sit immediately below and above the Mn ore intervals (Fig. 6j).

4.2.5. Carbon, sulfur, and molybdenum isotopes

Manganese ore samples have predominantly negative $\delta^{13}\text{C}_{\text{carb}}$ values that range from -22.33‰ to 0.16‰ , with an average of -11.55‰ . Conversely, micrite samples are characterized by a very narrow range of positive $\delta^{13}\text{C}_{\text{carb}}$ values between 4.21‰ and 4.75‰ , with an average of 4.58‰ .

Black shale and Mn ore intervals display distinct sulfide sulfur and bulk-rock Mo isotopic characteristics (Fig. 6f, h). The $\delta^{34}\text{S}_{\text{sulfide}}$ values of the black shale intervals vary between -25.24‰ and -9.16‰ , with an average of -16.30‰ . The Mn ore intervals possess heavier sulfide sulfur isotopic compositions, with $\delta^{34}\text{S}_{\text{sulfide}}$

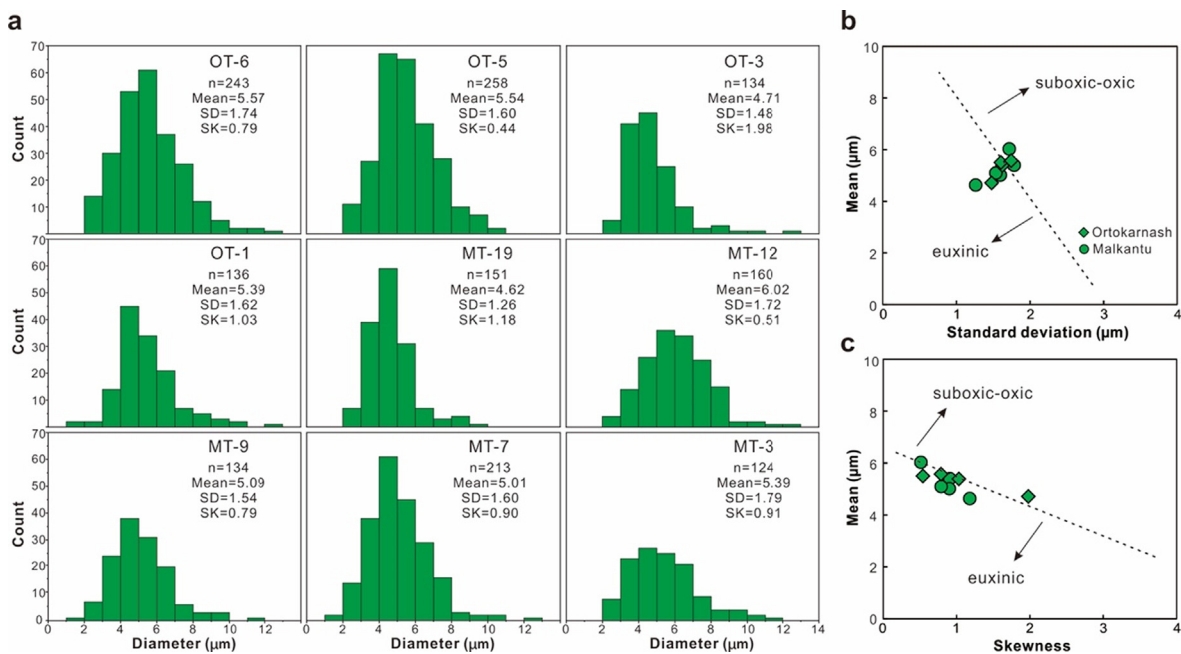


Fig. 5. (a) Size distribution patterns of pyrite framboids from the Ortokarnash and Malkantu black shales (SD: standard deviation; SK: skewness). See Table S1 for detailed dataset. (b–c) Mean diameter versus standard deviation (b) and skewness (c) for pyrite framboids from the Malkansu black shale samples. The dashed lines separate euxinic from suboxic-oxic water column conditions (cf. Wilkin et al., 1996).

values ranging from -11.19‰ to 5.92‰ , with an average of -0.31‰ (Fig. 6f). Regarding Mo isotopes, black shale intervals yield overall positive $\delta^{98}\text{Mo}_{\text{NIST}+0.25}$ values, from 0.07‰ to 1.32‰ except for a few negative outliers near 0‰ . In stark contrast, Mn ore intervals possess consistently negative $\delta^{98}\text{Mo}_{\text{NIST}+0.25}$ values that vary greatly between -2.58‰ and -0.28‰ , with an average of -1.07‰ (Fig. 6h).

5. Discussion

5.1. Origin of the Mn carbonate ores

The presence of Mn oxide inclusions within rhodochrosite (Zhang et al., 2020a) and the intergrowths of rhodochrosite with alabandite (Fig. 3c), a mineral that is typically indicative of a diagenetic environment (e.g., Burke and Kemp, 2002; Dong et al., 2022), suggest that the Mn carbonate minerals are likely the diagenetic product of primary Mn oxide reduction. Note that for alabandite to precipitate from a natural water, conditions must intersect a relatively small stability field with very low Eh (-0.5 – -0.7) and unusually high pH (greater than 11) conditions (Hem, 1972; Hein et al., 1999), making water column precipitation unlikely. Other sulfide minerals, such as pyrite (Fig. 3d) and (Co-Ni)-rich sulfide (Fig. 3e), occur as subhedral-euhedral grains up to $20\text{ }\mu\text{m}$ in size and are intergrown with Mn carbonate minerals, further suggesting a diagenetic origin of these sulfide minerals (e.g., Okita, 1992; Yan et al., 2020).

The geochemical and isotopic signatures of Mn carbonate ores have been commonly used to constrain their origin and depositional environments. Generally, however, a careful evaluation of syn-depositional processes (i.e., detrital contamination) on these features is required before using the geochemical and isotopic signatures (e.g., Chisonga et al., 2012; Xiao et al., 2017; Dong et al., 2022). The absence of detrital silicate minerals, along with the very low Al abundance (generally $<1.0\text{ wt}\%$) – an element that is typi-

cally diagnostic of clastic contamination (Tribouillard et al., 2006) – within the Malkansu Mn carbonate ores, indicates that detrital contamination was negligible during Mn deposition. Using the average total REE and Ce anomaly values of the Malkansu black shales as an endmember, a simple binary mixing model was used to further evaluate the detrital contribution. As shown in the Fig. 8, although detrital effects on both REE contents and Ce anomalies can be discerned in some Mn carbonate ore samples, chemical precipitation of primary Mn oxides with a strong scavenging effect still played a dominant role in controlling these features. In addition, the mixing curves also show that the platform micrite are rather pure with a negligible detrital component. There is also no correlation between Mo isotopes and Al contents for the Mn ore samples, together with the markedly high authigenic enrichment factors of Mo (average of 93), ruling out the possibility that detrital input has a significant effect on the Mo isotopic signature of the Mn ore samples.

The $\delta^{13}\text{C}$ values of Mn carbonate ore samples (-22.33‰ to 0.16‰) are much lower than those of the broadly coeval platform micrite (4.21‰ to 4.75‰), and that of the contemporaneous global ocean ($\sim 4\text{‰}$; Chen et al., 2018). Given the depleted carbon isotopic composition of organic matter preserved in the Malkansu Mn ore-bearing succession ($\delta^{13}\text{C} \approx -25\text{‰}$; Zhang et al., 2020a), there should be a significant contribution of organic-derived CO_2 to the formation of Mn carbonate minerals during diagenesis (e.g., Okita et al., 1988; Zhang et al., 2020a; Huang et al., 2022). This interpretation is further supported by the inverse correlation between $\delta^{13}\text{C}$ values and Mn contents (Fig. 9).

Manganese carbonate ore intervals show conspicuously higher authigenic enrichment factors of trace metals (e.g., Co, Ni, Mo) compared to those of the associated black shales (Fig. 6g). This may be attributable to the effective adsorption of trace metals to the precursor Mn oxides due to their negatively charged, reactive surface and large surface area (Bonatti et al., 1972; Post, 1999; Hein et al., 2013). Once these Mn oxides were buried and reduced

Table 1
Geochemical and isotopic results for Mn ore, black shale, and micrite samples from the Malkansu Mn metallogenic zone.

Sample No.	Lithology	Mn	Fe _T	Mn/Fe _T	Si	Al	Ca	TOC	S _{sulfide}	δ ³⁴ S _{sulfide}	δ ¹³ C _{carb}	Fe _{HR} /Fe _T	Fe _{py} /Fe _{HR}	Mo	Mo _{EF}	δ ⁹⁸ Mo _{NIST+0.25}	2SE	Ce/Ce*	
		wt%	wt%		wt%	wt%	wt%	wt%	wt%	‰	‰			ppm		‰			
Ortokarnash																			
OT-16	black shale	0.09	3.2	0.03	23.0	5.4	10.2	1.7	1.1	-19.52	n.a.	0.52	0.50	22.05	34	0.98	0.05	1.0	
OT-15	black shale	0.1	3.5	0.03	24.4	5.8	7.8	1.3	1.2	-22.60	n.a.	0.69	0.43	19.90	29	0.80	0.05	1.1	
OT-14	black shale	0.5	2.6	0.2	26.7	4.1	8.6	1.1	1.4	-20.19	n.a.	0.69	0.71	5.91	12	-0.10	0.05	0.8	
OT-13	black shale	0.3	3.0	0.1	25.5	6.7	6.5	1.5	1.1	-15.28	n.a.	0.48	0.69	14.53	18	0.79	0.04	0.9	
OT-12	Mn ore	40.8	0.4	91	2.8	0.4	2.2	0.5	0.02	3.55	-17.12	n.a.	n.a.	7.58	180	-0.97	0.05	3.5	
OT-11	Mn ore	40.0	0.6	64	2.0	1.0	2.1	0.6	0.2	5.49	n.a.	n.a.	n.a.	3.97	35	-0.61	0.10	3.5	
OT-10	Mn ore	39.6	1.2	33	4.6	1.3	1.0	0.4	0.3	3.20	-16.56	n.a.	n.a.	6.00	40	-0.46	0.06	3.4	
OT-9	Mn ore	43.0	0.7	65	3.0	0.7	1.1	0.4	0.1	5.27	n.a.	n.a.	n.a.	6.27	71	-0.28	0.07	3.6	
OT-8	Mn ore	39.8	1.1	37	4.3	2.0	0.8	0.3	0.1	-1.31	n.a.	n.a.	n.a.	1.22	5	-2.58	0.07	3.2	
OT-7	Mn ore	43.2	0.8	56	3.3	0.6	1.0	0.4	0.3	1.48	-22.33	n.a.	n.a.	4.69	67	-0.69	0.07	3.1	
OT-6	black shale	1.3	3.7	0.3	23.7	6.3	6.4	1.2	3.0	-9.16	n.a.	0.80	0.86	18.59	25	0.16	0.04	0.9	
OT-5	black shale	0.8	2.9	0.3	23.6	6.0	8.4	1.2	1.8	-15.08	n.a.	0.69	0.80	17.88	25	-0.08	0.04	1.0	
OT-4	black shale	0.6	4.2	0.1	24.3	6.2	6.8	1.2	3.4	-12.88	n.a.	0.82	0.87	12.44	17	0.49	0.04	1.0	
OT-3	black shale	0.9	1.6	1	24.2	4.0	11.4	0.9	0.7	-18.05	n.a.	0.53	0.68	15.49	32	0.48	0.06	1.0	
OT-2	black shale	0.9	4.8	0.2	18.9	4.6	11.0	0.5	1.3	-13.80	n.a.	0.32	0.74	1.97	4	0.48	0.04	1.2	
OT-1	black shale	1.1	4.3	0.2	15.8	5.7	14.2	0.6	1.0	-12.94	n.a.	0.31	0.64	3.89	6	1.32	0.05	0.8	
Malkantu																			
MT-20	black shale	0.1	2.7	0.04	33.6	6.1	0.6	2.7	2.0	-11.61	n.a.	0.78	0.84	26.17	36	-0.32	0.05	1.0	
MT-19	black shale	0.1	1.4	0.04	21.8	2.7	16.4	1.3	1.0	-13.90	n.a.	0.88	0.75	10.92	33	-0.09	0.06	1.0	
MT-18	black shale	0.1	1.6	0.03	23.2	2.9	14.7	1.5	1.2	-15.51	n.a.	0.87	0.77	10.82	32	-0.06	0.05	1.0	
MT-17	black shale	1.4	0.7	2	4.2	0.7	33.5	0.5	0.6	-9.34	n.a.	1.00	0.74	5.00	63	0.07	0.05	0.8	
MT-16	black shale	0.04	2.7	0.02	29.4	6.2	3.5	4.4	1.3	-18.74	n.a.	0.53	0.78	21.73	29	1.20	0.06	1.0	
MT-15	Mn ore	15.7	1.6	10	2.6	0.7	18.9	0.9	1.0	2.43	-5.08	n.a.	n.a.	14.88	180	-0.80	0.03	2.6	
MT-14	Mn ore	27.7	0.7	40	4.6	0.9	9.1	0.6	0.5	5.92	-3.79	n.a.	n.a.	30.70	283	-0.84	0.08	1.5	
MT-13	Mn ore	35.6	0.6	58	6.0	0.5	3.3	0.4	0.2	-11.19	-11.98	n.a.	n.a.	9.37	149	-1.77	0.04	3.6	
MT-12	black shale	0.04	3.5	0.01	27.2	7.6	3.0	4.9	2.2	-17.17	n.a.	0.62	0.86	28.39	31	1.17	0.07	1.1	
MT-11	black shale	0.1	2.0	0.07	19.1	3.1	17.2	2.1	1.0	-15.51	n.a.	0.65	0.68	12.02	32	1.05	0.04	1.0	
MT-10	black shale	0.03	3.1	0.01	32.7	4.4	2.8	1.8	1.6	-14.42	n.a.	0.57	0.78	12.44	24	1.22	0.05	0.9	
MT-9	black shale	1.7	2.7	1	11.1	4.3	17.7	0.7	1.8	-18.00	n.a.	0.99	0.57	5.83	11	0.87	0.08	0.9	
MT-8	black shale	3.6	2.8	1	16.7	4.9	11.9	0.8	1.4	-19.43	n.a.	0.63	0.66	4.15	7	0.25	0.05	0.9	
MT-7	black shale	4.2	3.0	1	18.5	5.4	7.8	1.0	1.4	-12.00	n.a.	0.66	0.61	8.21	13	0.36	0.05	0.9	
MT-6	Mn ore	18.3	1.9	10	12.7	0.6	9.4	0.5	1.6	-8.98	0.16	n.a.	n.a.	2.15	29	-0.98	0.04	1.2	
MT-5	Mn ore	41.3	0.5	79	2.1	0.3	1.9	0.7	0.3	-7.10	-14.20	n.a.	n.a.	1.23	34	-1.81	0.06	3.8	
MT-4	Mn ore	40.4	0.4	100	1.8	0.6	2.5	0.8	0.0	-2.49	-13.08	n.a.	n.a.	2.90	43	-1.10	0.08	3.5	
MT-3	black shale	0.1	2.9	0.03	25.0	5.9	7.5	2.1	1.2	-22.85	n.a.	0.48	0.77	19.91	28	-0.06	0.04	1.0	
MT-2	black shale	0.1	3.1	0.04	29.4	5.3	4.4	2.2	0.5	-18.03	n.a.	0.81	0.65	7.07	11	0.86	0.05	1.0	
MT-1	black shale	0.4	0.9	0.42	13.2	2.1	24.3	0.9	1.5	-25.24	n.a.	0.52	0.80	7.55	30	-0.10	0.05	0.8	
Kalaate																			
KL-6	micrite	0.01	0.05	0	0.6	0.03	39.1	n.a.	n.a.	n.a.	4.75	n.a.	n.a.	0.15	44	n.a.	n.a.	0.2	
KL-5	micrite	0.01	0.04	0	0.6	0.05	39.0	n.a.	n.a.	n.a.	4.82	n.a.	n.a.	0.27	47	n.a.	n.a.	0.2	
KL-4	micrite	0.04	0.06	1	0.4	0.06	39.4	n.a.	n.a.	n.a.	4.81	n.a.	n.a.	0.25	37	n.a.	n.a.	0.2	
KL-3	micrite	0.01	0.05	0	0.4	0.05	39.2	n.a.	n.a.	n.a.	4.21	n.a.	n.a.	0.04	6	n.a.	n.a.	0.2	
KL-2	micrite	0.02	0.07	0	0.7	0.08	39.0	n.a.	n.a.	n.a.	4.37	n.a.	n.a.	0.10	10	n.a.	n.a.	0.1	
KL-1	micrite	0.01	0.03	0	0.5	0.09	38.6	n.a.	n.a.	n.a.	4.49	n.a.	n.a.	0.09	6	n.a.	n.a.	0.1	

"n.a." denotes that this item was not analyzed.

during diagenesis, adsorbed trace metals might be liberated to form diagenetic minerals such as the (Co, Ni)-rich sulfides observed in the Mn ores (Fig. 3e) (cf. Okita, 1992).

Modern observations (Barling and Anbar, 2004; Goto et al., 2020) and laboratory experiments (Wasylenki et al., 2008, 2011) have shown that Mn oxides are the primary drivers of marine Mo isotopic fractionation, as they preferentially adsorb isotopically light Mo from seawater in the form of molybdate anions (MoO₄²⁻). This results in Mn oxides with a lighter Mo isotope value, and seawater with a heavier Mo isotope value, the latter of which tends to be recorded by black shales (Arnold et al., 2004; Dickson, 2017). Therefore, the Mo stable isotope systematics are a promising indicator for tracking the extent of Mn oxide burial (e.g., Scott and Lyons, 2012; Planavsky et al., 2014; Ossa et al., 2018; Goto et al., 2021). The average Mo isotopic value of Mn carbonate ore samples (-1.07 ‰ ± 0.66 ‰, 1SD, n = 12) is comparable to that of modern hydrogenous Mn oxide nodules (average = -0.65 ‰ ± 0.09 ‰, 1SD, n = 3; Goto et al., 2020), but markedly lower than that of the associated black shales (average = 0.49 ‰ ± 0.52 ‰, 1SD,

n = 24) (Fig. 6h), further supporting the Mn carbonate ores forming through the diagenetic reduction of primary Mn oxides.

Additionally, Mn oxides play a significant role in controlling marine REE distributions. In the modern oxygenated oceans, Mn oxides not only catalyze the surface oxidation of dissolved Ce(III) to immobile Ce(IV) leading to its preferential removal from seawater (Bau et al., 2014), but also scavenge Ho from seawater more quickly than Y due to the higher surface complexation stability of Ho (Nozaki et al., 1997). As a result, modern hydrogenous Mn nodules exhibit positive Ce anomalies, negative Y anomalies, and lower Y/Ho ratios relative to the PAAS shale composite (~27; Taylor and McLennan, 1985) and modern seawater (~44; Bolhar et al., 2004). The Mn carbonate ore samples show strikingly similarities to modern hydrogenous Mn nodules with respect to REE patterns (Fig. 7), namely they display highly positive Ce anomalies (1.2–3.8; average = 3.0), slightly negative Y anomalies (0.8–1.3; average = 0.9), and low Y/Ho ratios (22–35; average = 25), consistent with a diagenetic origin for the Mn carbonate ores through reduction of Mn oxides (e.g., Gutzmer and Beukes, 1998; Xiao

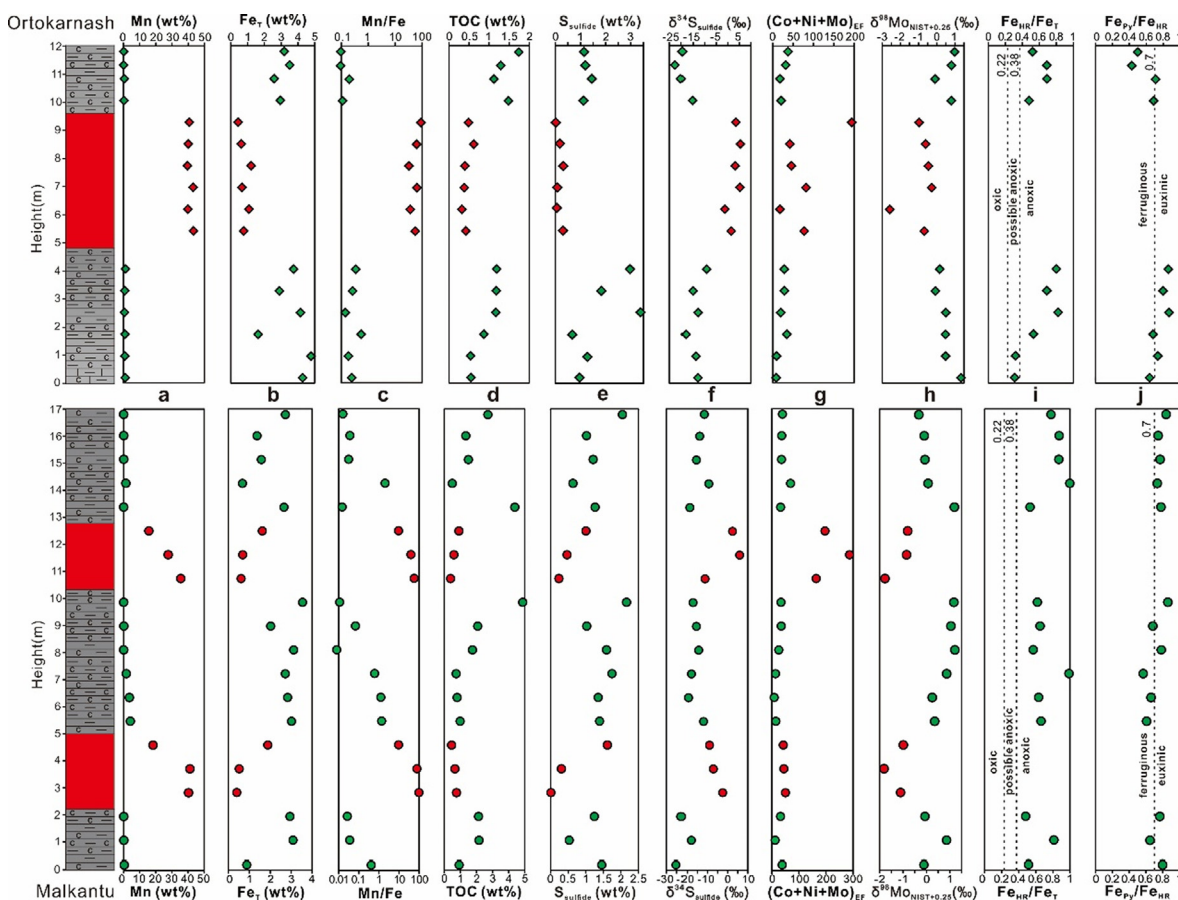


Fig. 6. Chemostratigraphic profiles of selected geochemical and isotopic compositions for both Ortokarnash and Malkantu sections. The dashed lines in i and j are the thresholds utilized in Fe speciation systematics (Poulton and Canfield, 2011). Lithological legends are the same as Fig. 2.

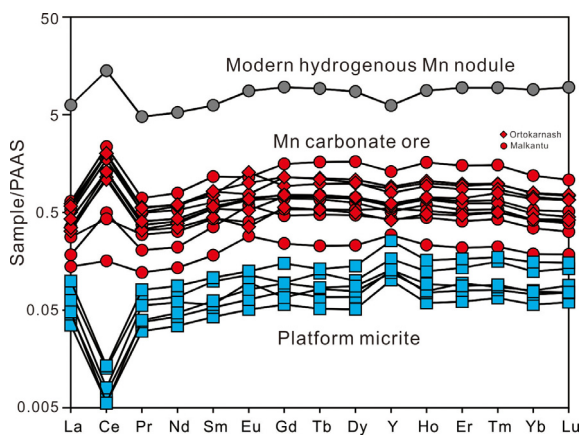


Fig. 7. PAAS-normalized rare earth elements (REE) patterns of Mn carbonate ore and platform micrite samples from the Malkantu area. Also shown is the typical REE pattern of modern hydrogenous Mn nodules (Bau et al., 2014).

et al., 2017; Zhang et al., 2020a). These features also suggest that initial sedimentary Mn enrichments (greater than 30 wt%) were developed under a fully oxygenated water column rather than a redox-stratified water column characterized by Mn oxide cycling near the redoxcline (e.g., Herndon et al., 2018; Wittkop et al., 2020). Although the latter scenario can also generate positive Ce anomalies due to shuttled Mn oxides undergoing reduction, the Ce anomalies generated via this pathway are generally small and are decoupled from significant sedimentary Mn enrichments

(e.g., Tostevin et al., 2016; Wu et al., 2019). Further, the Ce-rich authigenic monazite observed within the Mn ores (Fig. 3f–h) would likely represent the main phase hosting Ce liberated during the reduction of precursor Mn oxides, providing additional support for the diagenetic origin of Mn carbonate ores.

5.2. Redox structure before and after Mn deposition

The Malkantu black shales contain abundant framboidal pyrite with no evidence of post-depositional oxidation (Fig. 4e–i), as also confirmed by their lack of Ce anomalies (cf. Planavsky et al., 2020; Zhang and Shields, 2022). Therefore, the size distribution of framboidal pyrites can be used to infer benthic redox conditions during deposition (e.g., Bond and Wignall, 2010; Shen et al., 2016; Grasby et al., 2021). Based on the analysis of pyrite framboid size distributions in modern sediments, syngenetic framboids with mean diameters of <5 μm are indicative of pyrite forming in euxinic bottom waters (Wilkin et al., 1996,1997). Pyrite framboids formed in euxinic waters are also generally less variable in size than diagenetic framboids formed within oxic-suboxic sediments, because the former tends to develop relatively quickly (Wilkin et al., 1996; 1997). For the Malkantu black shale samples, more than 1500 framboids were measured with overall mean sizes between 4 and 6 μm, and a narrow range (standard deviations <2 μm) (Fig. 5a), suggesting a syngenetic origin and predominantly euxinic bottom water conditions during deposition (Fig. 5b, c). Consistent with this interpretation, framboidal pyrites in the Malkantu black shales are smaller than diagenetic pyrites in the Mn ores (~20 μm; Fig. 3d), and they have lighter sulfur

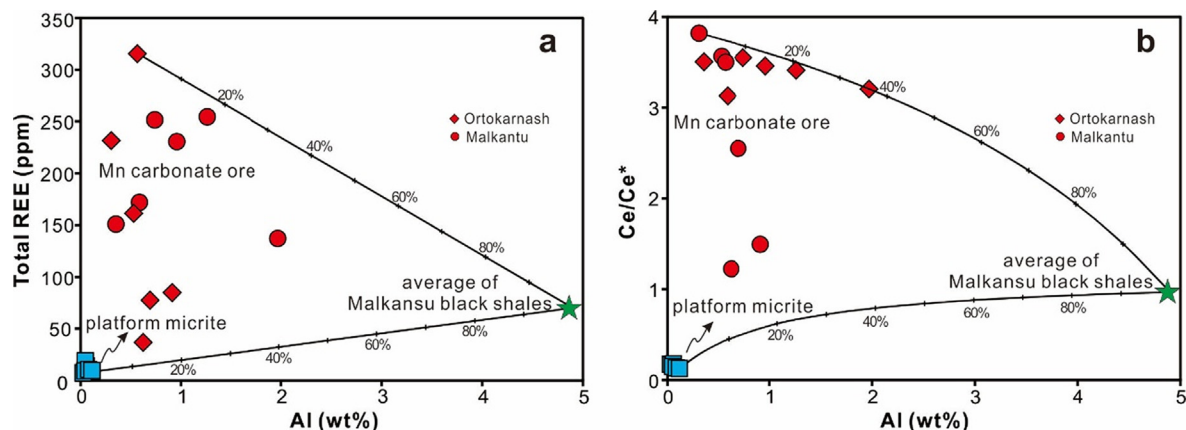


Fig. 8. Binary mixing curves between Malkansu black shales and Mn ores, as well as platform micrites, with respect to total REE concentration (a) and Ce anomaly (b). The average total REE concentration and Ce anomaly values of the Malkansu black shales are considered to be reflective of the detrital endmember.

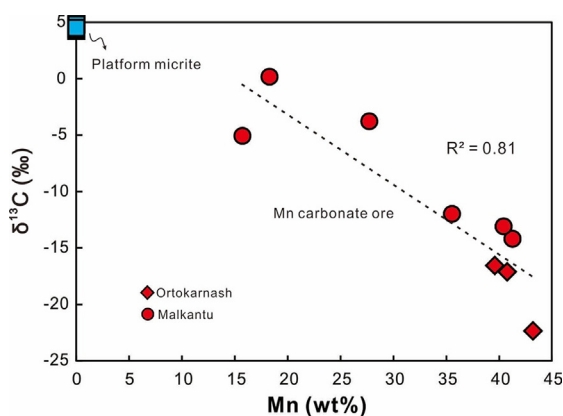


Fig. 9. Carbon isotope values plotted against Mn contents for the Mn carbonate ore samples. Also shown are the carbon isotope values of the contemporaneous platform micrites (blue squares).

isotopic compositions (average $\delta^{34}\text{S}_{\text{sulfide}}$ of -16.30‰) relative to the Mn ores (average $\delta^{34}\text{S}_{\text{sulfide}}$ of -0.31‰) (Fig. 6f). These sulfur isotopic trends indicate that pyrite in the black shales was precipitated from bottom water columns with greater sulfate availability relative to diagenetic pore waters, thereby resulting in a larger fractionation between aqueous sulfate and the sulfide minerals (e.g., Okita and Shanks, 1992; Polgári et al., 2016; Emmings et al., 2020; Gilleaudeau et al., 2021).

Iron speciation of fine-grained siliciclastic rocks has been commonly used as a powerful proxy for reconstructing past ocean redox states, since the geochemical cycling of iron near the sediment–water interface is highly dependent on benthic redox conditions (Poulton and Canfield, 2011; Raiswell et al., 2018). Generally, $\text{Fe}_{\text{HR}}/\text{Fe}_{\text{T}}$ ratios above 0.38 are characteristic of anoxic deposition and ratios below 0.22 are indicative of oxic conditions, with intermediate values (0.22–0.38) being considered equivocal (Poulton and Canfield, 2011). Additionally, the extent of highly reactive iron that is pyritized in anoxic sediments ($\text{Fe}_{\text{py}}/\text{Fe}_{\text{HR}}$) can aid in distinguishing euxinic and ferruginous depositional conditions. It is proposed that $\text{Fe}_{\text{py}}/\text{Fe}_{\text{HR}}$ ratios exceeding 0.7 are indicative of euxinic bottom water conditions for Phanerozoic sediments (März et al., 2008; Raiswell et al., 2018). The Malkansu black shale samples yield $\text{Fe}_{\text{HR}}/\text{Fe}_{\text{T}}$ ratios greater than 0.38 except for two that fall within the equivocal range. Coupled with $\text{Fe}_{\text{py}}/\text{Fe}_{\text{HR}}$ ratios mostly greater than 0.7 (especially foot-wall samples near the Mn ore intervals) (Fig. 6j), the black shales record unambiguously euxinic

and dominantly euxinic depositional conditions, consistent with the seafloor euxinia as inferred from the pyrite framboid size distributions (Fig. 5b, c).

Based on the covariant patterns of redox-sensitive elements including Mo and U, we can further probe the water column redox structure during black shale deposition. Although both tend to be enriched in sediments under reducing conditions (Tribovillard et al., 2006), some differential geochemical behavior can result in distinct authigenic enrichment levels. First, authigenic U sequestration commences under suboxic conditions (Zheng et al., 2002; Algeo and Li, 2020), while authigenic Mo enrichment requires H_2S in bottom waters (i.e., euxinic conditions) (Helz et al., 2011; Scott and Lyons, 2012). More importantly, Mo has a higher affinity for adsorption onto Mn oxide particles than U (Klinkhammer and Palmer, 1991; Algeo and Tribovillard, 2009). The shuttling of Mn oxides across an oxic–euxinic interface within the water column therefore has the potential to accelerate the transfer of Mo into the sediments, leading to a stronger authigenic enrichment in Mo relative to U, as observed in the modern Cariaco Basin (Algeo and Tribovillard, 2009; Tribovillard et al., 2012). The Malkansu black shale samples display a stronger authigenic Mo enrichment than U and yield a covariant Mo–U pattern typical of that generated through an active Mn oxide particulate shuttle (Fig. 10), providing evidence for redox cycling of Mn within the water column. This further implies that the Malkansu basin was redox-stratified with deeper euxinic waters overlain by oxic surface waters (cf. Scholz et al., 2013). Oxic surface conditions are consistent with the roughly coeval platform micrite characterized by strongly negative Ce anomalies (Fig. 7). Moreover, the Mn particulate shuttle indicates that the depth of the redoxcline was relatively deep, probably fluctuating just above the sediment–water interface. Only under this scenario can the Mo released from Mn oxides upon reductive dissolution reach the sediments and then be sequestered by organic matter or pyrite (Algeo and Tribovillard, 2009; Little et al., 2015). It is noteworthy that black shale samples have only slightly higher Mn contents (average of 0.8 wt%) relative to those of the PAAS composite ($\sim 0.1\text{ wt}\%$; Taylor and McLennan, 1985), suggesting that re-dissolved Mn could not efficiently be fixed into sediments. The lack of an efficient Mn sink in black shales is likely due to the low affinity of sulfide minerals in euxinic bottom waters for Mn (e.g., Krauskopf, 1957; Ostrander et al., 2019; Lenstra et al., 2020).

Given that Mn oxides preferentially adsorb light Mo isotopes (Barling and Anbar, 2004; Wasylenki et al., 2008), an active Mn oxide shuttle in the Malkansu basin may have transferred isotopically light Mo into sediments, as observed in both modern

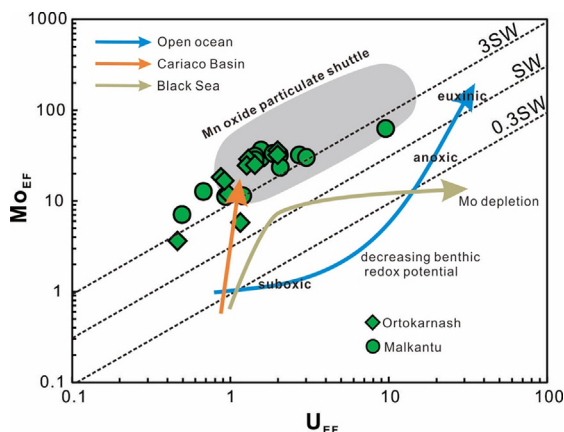


Fig. 10. Cross-plot of Mo_{EF} versus U_{EF} for the black shale samples indicating the presence of a Mn oxide particulate shuttle. Dashed lines represent multiples (0.3, 1, and 3) of the Mo/U ratio of the modern seawater (~ 3.1). Different metal enrichment pathways are indicative of different hydrographic and redox conditions. adapted from [Algeo and Tribouillard, 2009](#)

(e.g., [Noordmann et al., 2015](#); [Hardisty et al., 2016](#)) and ancient environments (e.g., [Ostrander et al., 2019](#); [Kendall et al., 2020](#)). The Mo isotope values of the Malkansu black shale samples vary greatly between -0.32‰ and 1.32‰ , below that of mid-Carboniferous seawater (minimum of 1.9‰ ; [Lu et al., 2020](#); [Dong et al., 2022](#)). This can be attributed to weakly euxinic bottom water conditions with H_2S concentrations below $11\ \mu M$, which would have led to an isotopic offset towards lower values than coeval seawater due to the formation of intermediate thiomolybdate species ($MoO_{4-x}S_x^{2-}$, $x = 1-4$) and non-quantitative Mo removal ([Tossell, 2005](#); [Kendall et al., 2017](#); [Dickson, 2017](#)). Although the magnitude of Mo isotopic fractionation associated with weakly euxinic deposition can be large (e.g., [Neubert et al., 2008](#); [Nägler et al., 2011](#)), a net negative offset of -0.7‰ is often observed ([Dahl et al., 2010](#); [Kendall et al., 2017](#); [Dickson, 2017](#)). Hence, the larger Mo isotopic offset of up to -2.2‰ between the Malkansu black shales and overlying seawater likely arose from intense Mn oxide shuttling, further verifying water-column redox stratification immediately before and after Mn deposition.

5.3. Depositional model

The Mn ore-bearing Kalaatehe Formation represents a sedimentary succession recording gradually deepening water depth due to basinal subsidence ([Zhang et al., 2020a](#); [Dong et al., 2020](#)). The lower breccia-bearing limestone (Member 1) and sandy limestone (Member 2) were deposited in a shallow and oxic basin ([Fig. 11a](#)), consistent with the presence of bioclasts and negative Ce anomalies observed in these carbonate rocks ([Zhang et al., 2020a](#)). The overlying Member 3 is composed of finely-laminated organic-rich black shales ([Fig. 4a, b](#)) and intercalated Mn ore layers, suggesting deposition in a deeper, low-energy environment ([Zhang et al., 2020a](#); [Dong et al., 2020](#)). Based on the presence of Mn oxide relics enclosed by Mn carbonates and highly negative carbon isotope values of Mn carbonates, [Zhang et al. \(2020a\)](#) also proposed a diagenetic origin for the Ortokarnash Mn deposit. Further, they suggested that the whole Kalaatehe Formation was deposited under an oxic water column given their negative (limestones of Member 1 and Member 2) and positive Ce anomalies (Mn ores in the Member 3). In this context, a “bathtub-ring” model was speculated for the Ortokarnash Mn deposit. It should be noted that, however, that the black shales of the Member 3 do not have Ce anomalies, likely implying that they were deposited under different redox conditions relative to the other rock types.

Utilizing the Fe speciation systematics and the size distribution pattern of framboidal pyrites, this study focuses on black shales associated with two typical Mn deposits (Ortokarnash in the west and Malkantu in the east) of the Malkansu Mn metallogenic zone, and aims to provide new insights into the redox conditions contemporaneous to their deposition. The results reveal that the Malkansu black shales were deposited under euxinic bottom waters ([Fig. 5b, c](#); [Fig. 6i, j](#)). Therefore, Member 3 actually records a deep-water euxinic condition, punctuated by episodes of benthic oxygenation (i.e., Mn ore intervals). Additionally, it is noteworthy that the nearly synchronous thin-bedded platform micrites were deposited in oxic water columns, as indicated by their highly negative Ce anomalies ([Fig. 7](#)). Taken together, the deep-water euxinic settings where black shales were deposited, coupled with oxic conditions that prevailed in the shallower platform portion of the basin, imply that continued tectonic subsidence resulted in the formation of a redox-stratified basin ([Fig. 11b](#)). This redox stratification might be caused by limited exchange of water masses between the depositional basin and the open ocean. Such an interpretation can be further verified by the sedimentary Mo/TOC ratios, a proxy that has been widely used to evaluate the degree of basin restriction (e.g., [Algeo and Rowe, 2012](#); [Mänd et al., 2020](#); [Gilleaudeau et al., 2021](#)). The Malkansu black shale samples yield Mo/TOC ratios (9 ± 4 , 1SD, $n = 24$) between that of the strongly restricted Black Sea (~ 4.5) and intermittently restricted Cariaco Basin (~ 25) ([Fig. 12a](#)), indicating a sluggish deep-water renewal and a limited Mo replenishment from open seawater during deposition of black shales (cf. [Algeo and Lyons, 2006](#)). In addition, black shales deposited beneath euxinic waters replete with Mo generally have Mo concentrations above 100 ppm ([Scott and Lyons, 2012](#)). However, the Malkansu black shales do not show conspicuous Mo enrichments (average of 13 ppm), although they were deposited under euxinic bottom waters. This also suggests an insufficient Mo replenishment caused by hydrographic restriction in the Malkansu basin ([Fig. 12b](#)) (cf. [Bauer et al., 2022](#)).

It should be noted that there are some chalcedony laminae within the black shales in places ([Fig. 4c, d](#)), which are similar to submarine exhalative silica-rich layers commonly observed in black shales (e.g., [Steiner et al., 2001](#); [Zhou et al., 2014](#); [Xie et al., 2021](#)). These might reflect intermittent hydrothermal inputs during deposition, as indicated by the negative $\epsilon Nd(t)$ values of the black shales suggesting the influence of seafloor hydrothermal fluids that were derived from interaction with old continental basement ([Zhang et al., 2022](#)). This hydrothermal activity could also have introduced Mn into the euxinic bottom waters, as Mn can be enriched up to a million fold over ambient seawater in modern submarine hydrothermal systems (e.g., [Von Damm et al., 1985](#); [Schmidt et al., 2003](#)). Given that Mn does not readily form sulfide minerals relative to Fe ([Krauskopf, 1957](#)), euxinic bottom waters would have facilitated the accumulation of Mn, and fostered the near complete separation of Mn from Fe via deposition of pyritic black shales. This is reflected by significantly lower Mn/Fe ratios in the black shales (average of 0.3) than in the Mn ores (average of 53) ([Fig. 6c](#)), as well as the occurrence of alabandite in the Mn ores ([Fig. 3c](#)), which indicates the existence of a Mn-rich, Fe-depleted water column (e.g., [Lepland et al., 1998](#); [Dong et al., 2022](#)).

The Mn ore beds intercalated with the black shales record abrupt redox shifts in bottom water conditions from euxinic to oxic ([Fig. 6](#)). This deep-water ventilation was likely induced by the periodic influxes of oxic seawater ([Fig. 11c](#)), consistent with the Mo isotopic compositions of Mn ore samples. Despite a large variation in the Mo isotope values of Mn ores (from -2.58‰ to -0.28‰), there is a cluster between -1.10‰ and -0.46‰ with an average of $-0.81\text{‰} \pm 0.21\text{‰}$ (1SD, $n = 8$). Although the adsorption of Mo to either Fe oxides ([Goldberg et al., 2009](#)) or organic matter ([King](#)

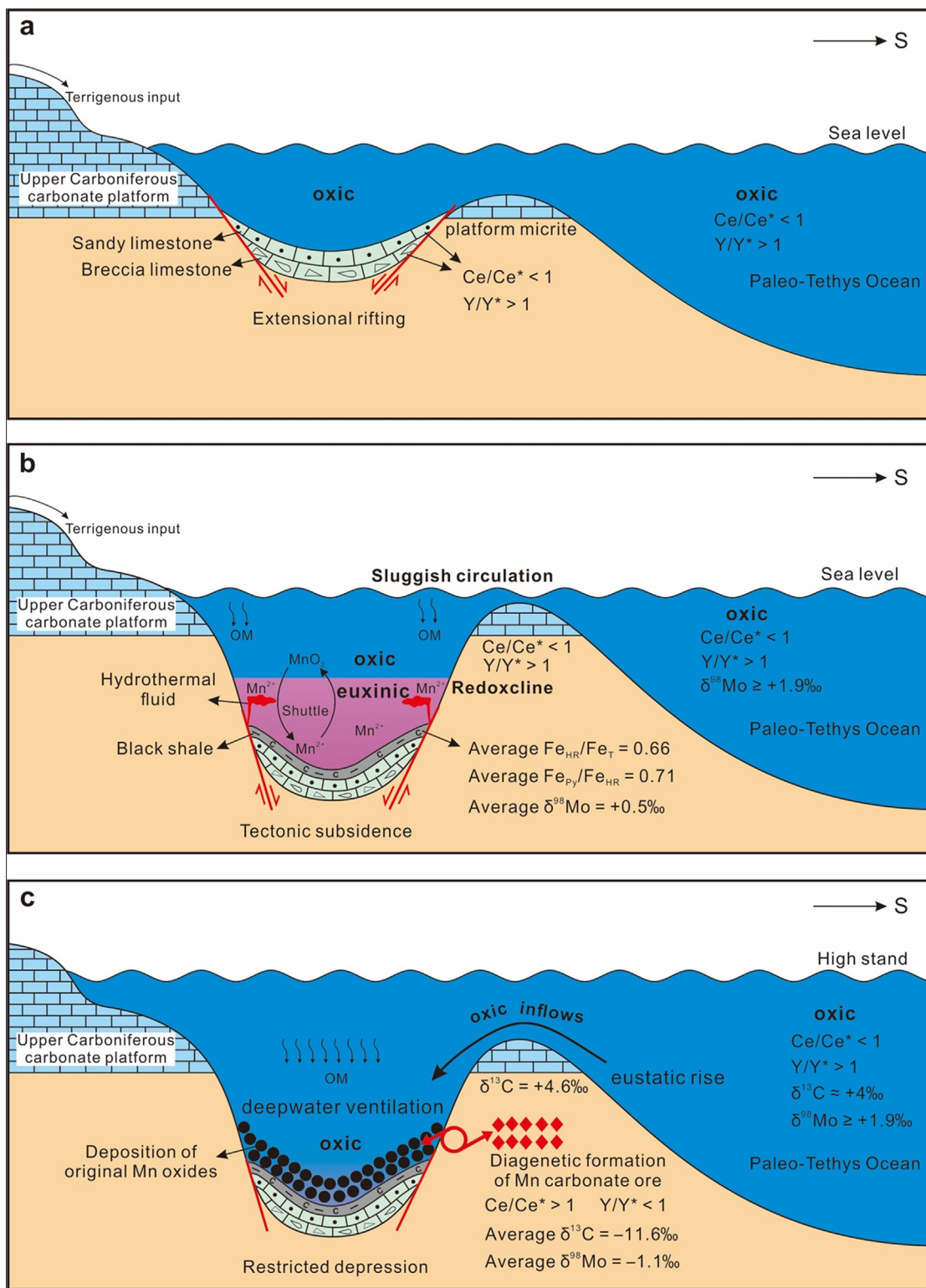


Fig. 11. Depositional model illustrating the sedimentary–diagenetic processes of the Malkansu Mn deposits. See the section 5.3. *Depositional model* for full details. Briefly, (a) the depositional basin prior to tectonic subsidence is characterized by oxic bottom water conditions. (b) Tectonic subsidence leads to the development of a redox-stratified basin with euxinic conditions at depth and an active Mn oxide shuttle. This hydrodynamic condition results in the accumulation of dissolved Mn in anoxic to euxinic bottom waters. (c) Periodic ventilation by the influxes of oxygenated seawater leads to the deposition of Mn oxides which subsequently are reduced through the coupled oxidation of organic matter, forming the Mn carbonate ore intervals. This depositional model accounts for the close association with black shale intervals and indicates that Mn ores may be developed at depth rather than on shallow basin margins.

et al., 2018) can also result in a preferential removal of light Mo isotopes into sediments, the absence of correlations between Mo isotope values and Fe contents and TOC contents suggests that

the Mo isotopic composition of Mn ores was predominantly controlled by the adsorption of Mn oxides rather than Fe oxides or organic matter. In this context, based on the constant

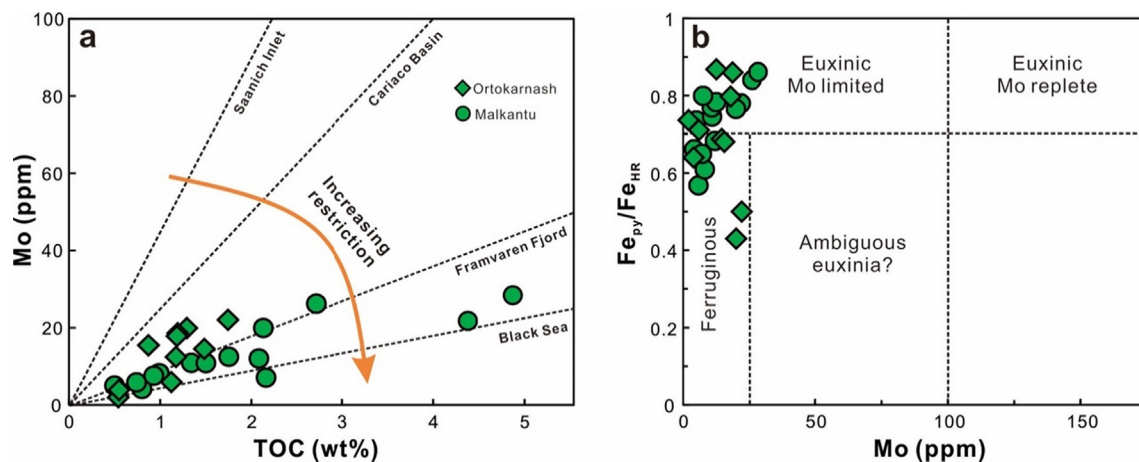


Fig. 12. (a) Cross-plot of Mo versus TOC for black shale samples indicating a relatively strong hydrographic restriction during deposition. Four modern silled basins with different degrees of restriction are shown for comparison (Algeo and Rowe, 2012). (b) Fe_{py}/Fe_{HR} versus Mo concentrations indicating that hydrographic restriction led to a limited Mo resupply during deposition of black shales (cf. Bauer et al., 2022).

equilibrium Mo isotopic fractionation factor (approximately -2.7‰) between Mn oxides and seawater over geologic time (Wasylenki et al., 2008; 2011), the Mo isotopic composition of waters from which original Mn oxides were deposited is likely to have been $1.89\text{‰} \pm 0.21\text{‰}$. This is broadly consistent with the Mo isotope value of mid-Carboniferous seawater (minimum of 1.9‰ ; Lu et al., 2020; Dong et al., 2022), thus supporting the hypothesis of bottom water ventilation due to periodic seawater incursions. This also suggests that ancient Mn-rich sediments are a reliable archive of seawater redox and chemistry evolution even following diagenesis (e.g., Goto et al., 2020). Note that there are also a few more depleted Mo isotope values (from -1.77‰ to -2.58‰) that likely reflect Mn oxide precipitation from localized hydrothermal fluids (e.g., Goto et al., 2021), because hydrothermally-derived Mo possesses markedly lower Mo isotope values than ambient seawater ($\sim 0.6\text{‰}$; McManus et al., 2002). In addition, the relatively enriched Mo isotope value (i.e., -0.28‰) in the Mn ore can be attributed to a direct addition of isotopically heavy hydrothermal Mo into pore waters during early diagenesis (e.g., Goto et al., 2021). Given the continued subsidence of the depositional basin, oxic inflows from the open ocean might be related to eustatic sea level rises. This is supported by the Mn ore depositional age of $\sim 320\text{ Ma}$ (Li et al., 2022) being broadly synchronous with an interglacial period of the Late Paleozoic ice age (LPIA; Ahern and Fielding, 2021), which was characterized by high-frequency and high-amplitude sea-level fluctuations (Isbell et al., 2012). We infer that the rising glacio-eustatic sea levels would have caused frequent deep-water renewal and continuous bottom water oxygenation (cf. Algeo and Rowe, 2012; Peng et al., 2021a).

Collectively, the multiple black shale-hosted Mn ore layers were formed by episodic hydrothermal activities and ventilation of euxinic bottom waters (Fig. 11b, c). This process is analogous to the formation mechanism for Mn carbonate laminae (up to 32 wt% Mn) hosted within organic-rich sapropels of the Baltic Sea (Huckriede and Meischner, 1996; Häusler et al., 2018). Real-time observations show that episodic oxic inflows from the Atlantic result in the recurring oxygenation of euxinic bottom waters and trigger precipitation of Mn oxides, which were diagenetically transformed into Mn carbonate and Mn sulfide minerals following burial (Dellwig et al., 2018; Häusler et al., 2018; Hermans et al., 2019).

Also note that many other Mn carbonate deposits over geologic record share similar stratigraphic characteristics and paleogeographic framework with the Malkansu Mn deposits. For instance, the Lower Jurassic Úrkút Mn deposit in Hungary shows an intimate stratigraphic association between Mn carbonate ore layers and black shales, a succession that has been assumed to be formed in intermittently restricted deep basins characterized by redox stratification (Jenkyns et al., 1991). Similarly, the established paleogeography shows that the Early Carboniferous black shale-hosted Mn carbonate deposits in the Rheno-Hercynian zone (Germany) are located in the deepest center of anoxic basins (Meischner, 1971). By analogy with the recent Baltic Sea, Huckriede and Meischner (1996) speculated that sporadic long-term oxidation of euxinic deep waters caused by oxic inflows is responsible for the formation of these Lower Jurassic and Lower Carboniferous Mn deposits in Europe. Moreover, the Neoproterozoic interglacial Datangpo Formation is well known for hosting black shale-associated Mn carbonate deposits, which formed in the deep parts of sub-basins rather than on the sub-basin margins of the Nanhua rifted Basin (Zhou et al., 2016). Therefore, Yu et al. (2016) proposed an “episodic ventilation” model where these Mn deposits were generated by intermittent density flows that carried oxygenated surface waters into the anoxic deep waters.

To sum up, we suggest that the “episodic ventilation” model should be viable for ancient black shale-hosted Mn carbonate deposits throughout Earth’s history. In contrast to the classic “bathtub ring” model (Force and Cannon, 1988), the ventilation model highlights deep-water Mn mineralization in the center rather than on the margin of restricted basins, where anoxic (especially euxinic) bottom waters are prone to sporadic ventilation. This ventilation might be driven by multiple processes, such as seawater influxes (e.g., this study; Robertson et al., 2019), meltwater incursions (e.g., Xu et al., 2019; Cai et al., 2022), density flows (e.g., Yu et al., 2016), or a combination of multiple hydrologic processes (Hein et al., 1999). Our study also confirms that large-scale and high-grade sedimentary Mn deposits appear to be formed in euxinic and restricted basins, which can facilitate the complete separation of Mn from Fe, as well as the accumulation of dissolved Mn before mineralization (Liu, 1990; Maynard, 2010; Hermans et al., 2019). In addition, the ventilation model sheds new light on the genesis of Mn-rich black shale successions, which likely reflects *in-situ* bottom water redox oscillations where anoxic

conditions were interrupted by periods of deep-water oxygenation (e.g., Planavsky et al., 2018).

6. Conclusions

The Malkansu Mn carbonate ore deposits are directly associated with organic-rich black shales that were deposited in a restricted, deeper-water, marine environment. During the deposition of black shales, the water column was redox-stratified with oxic surface waters overlying euxinic bottom waters. This promoted the near complete separation of Mn from Fe and facilitated the significant build-up of dissolved Mn(II). Episodic inflows of oxygenated seawater caused abrupt shifts in bottom water redox conditions from euxinic to oxic, triggering the massive accumulation of Mn(IV) oxides on the seafloor. Once buried, these primary Mn(IV) oxides were transformed into low-valence Mn(II) carbonate minerals such as rhodochrosite (and minor alabandite) through diagenetic reduction coupled to the oxidation of organic matter.

This study unravels the details of the complex temporal and spatial redox and hydrographic dynamics that resulted in Mn metallogenesis associated with black shales. We highlight that black shale-hosted Mn carbonate deposits might be formed by *in-situ* ventilation of anoxic (especially euxinic) bottom waters in relatively deep-water environments, rather than by the upwelling of anoxic deep waters onto shallow oxic basin margins.

Declaration of Competing Interest

The authors declare that they have no known competing financial interests or personal relationships that could have appeared to influence the work reported in this paper.

Data availability

The research data associated with this publication are included in the text and [supplementary material](#).

Acknowledgements

This study was supported by the National Natural Science Foundation of China (U1703242). WCL acknowledges additional support from the Key Research Program of Frontier Sciences, Chinese Academy of Sciences (ZDBS-LY-DQC037) and Youth Innovation Promotion Association, Chinese Academy of Sciences. ZBL acknowledges additional support from the Project funded by China Postdoctoral Science Foundation (2021M703018). The authors are grateful to Yue-Qiao Xie and Li-Dong He for their help with field work, as well as Hong-Wei Li, Jiang-Yan Yuan, Zi-Hu Zhang, and Zhi-Dan Wang for assistance with lab works. We also thank executive editor Jeffrey G. Catalano, associate editor Eva Stüeken, Dennis Kraemer, and two anonymous reviewers for their constructive comments, which helped improve earlier version of this manuscript.

Appendix A. Supplementary material

Supplementary material to this article can be found online at <https://doi.org/10.1016/j.gca.2022.11.027>.

References

Ahern, J.P., Fielding, C.R., 2021. Paleotropical climate oscillations from upper Mississippian and Pennsylvanian stratigraphic records of western Laurentia: A convolution of plate migration and Gondwanan ice dynamics. *Palaeogeogr. Palaeoclimatol. Palaeoecol.* 561, 110019.

- Algeo, T.J., Li, C., 2020. Redox classification and calibration of redox thresholds in sedimentary systems. *Geochim. Cosmochim. Acta* 287, 8–26.
- Algeo, T.J., Lyons, T.W., 2006. Mo–total organic carbon covariation in modern anoxic marine environments: Implications for analysis of paleoredox and paleohydrographic conditions. *Paleoceanography* 21, PA1016.
- Algeo, T.J., Rowe, H., 2012. Paleocceanographic applications of trace-metal concentration data. *Chem. Geol.* 324–325, 6–18.
- Algeo, T.J., Tribouillard, N., 2009. Environmental analysis of paleocceanographic systems based on molybdenum–uranium covariation. *Chem. Geol.* 268, 211–225.
- Arnold, G.L., Anbar, A.D., Barling, J., Lyons, T.W., 2004. Molybdenum isotope evidence for widespread anoxia in mid-proterozoic oceans. *Science* 304, 87–90.
- Arthur, M.A., Sageman, B.B., 1994. Marine black shales – depositional mechanisms and environments of ancient-deposits. *Annu. Rev. Earth Planet. Sci.* 22, 499–551.
- Barling, J., Anbar, A.D., 2004. Molybdenum isotope fractionation during adsorption by manganese oxides. *Earth Planet. Sci. Lett.* 217, 315–329.
- Bau, M., Schmidt, K., Koschinsky, A., Hein, J., Kuhn, T., Usui, A., 2014. Discriminating between different genetic types of marine ferro-manganese crusts and nodules based on rare earth elements and yttrium. *Chem. Geol.* 381, 1–9.
- Bauer, K.W., Bottini, C., Katsev, S., Jelinek, M., Francois, R., Erba, E., Crowe, S.A., 2022. Ferruginous oceans during OAE1a and collapse of the marine sulfate pool. *Earth Planet. Sci. Lett.* 578, 117324.
- Bekker, A., Planavsky, N.J., Krapež, B., Rasmussen, B., Hofmann, A., Slack, J.F., Rouxel, O.J., Konhauser, K.O., 2014. Iron Formations: Their Origins and Implications for Ancient Seawater Chemistry. In: Holland, H.D., Turekian, K.K. (Eds.), *Treatise on Geochemistry*. 2nd Edition. Elsevier, Oxford, pp. 561–628.
- Beukes, N.J., Swindell, E.P.W., Wabo, H., 2016. Manganese deposits of Africa. *Episodes* 39, 285–317.
- Bolhar, R., Kamber, B.S., Moorbath, S., Fedo, C.M., Whitehouse, M.J., 2004. Characterisation of early Archaean chemical sediments by trace element signatures. *Earth Planet. Sci. Lett.* 222, 43–60.
- Bonatti, E., Fisher, D.E., Joensuu, O., Rydell, H.S., Beyth, M., 1972. Iron-Manganese-Barium Deposit from the Northern Afar Rift (Ethiopia). *Econ. Geol.* 67, 717–730.
- Bond, D.P.G., Wignall, P.B., 2010. Pyrite framboid study of marine Permian-Triassic boundary sections: A complex anoxic event and its relationship to contemporaneous mass extinction. *Geol. Soc. Am. Bull.* 122, 1265–1279.
- Browning, T.J., Achterberg, E.P., Engel, A., Mawji, E., 2021. Manganese co-limitation of phytoplankton growth and major nutrient drawdown in the Southern Ocean. *Nat. Commun.* 12, 884.
- Burke, I.T., Kemp, A.E.S., 2002. Microfabric analysis of Mn-carbonate laminae deposition and Mn-sulfide formation in the Gotland Deep, Baltic Sea. *Geochim. Cosmochim. Acta* 66, 1589–1600.
- Cai, C.F., Lyons, T.W., Sun, P., Liu, D.W., Wang, D.W., Tino, C.J., Luo, G.M., Peng, Y.Y., Jiang, L., 2022. Enigmatic super-heavy pyrite formation: Novel mechanistic insights from the aftermath of the Sturtian Snowball Earth. *Geochim. Cosmochim. Acta* 334, 65–82.
- Calvert, S.E., Pedersen, T.F., 1996. Sedimentary geochemistry of manganese: Implications for the environment of formation of manganeseiferous black shales. *Econ. Geol.* 91, 36–47.
- Canfield, D.E., Raiswell, R., Westrich, J.T., Reaves, C.M., Berner, R.A., 1986. The use of chromium reduction in the analysis of reduced inorganic sulfur in sediments and shales. *Chem. Geol.* 54, 149–155.
- Chen, J.T., Montañez, I.P., Qi, Y.P., Shen, S.Z., Wang, X.D., 2018. Strontium and carbon isotopic evidence for decoupling of pCO₂ from continental weathering at the apex of the late Paleozoic glaciation. *Geology* 46, 395–398.
- Chisonga, B.C., Gutzmer, J., Beukes, N.J., Huizenga, J.M., 2012. Nature and origin of the protolith succession to the Paleoproterozoic Serra do Navio manganese deposit, Amapa Province, Brazil. *Ore Geol. Rev.* 47, 59–76.
- Dahl, T.W., Hammarlund, E.U., Anbar, A.D., Bond, D.P.G., Gill, B.C., Gordon, G.W., Knoll, A.H., Nielsen, A.T., Schovsbo, N.H., Canfield, D.E., 2010. Devonian rise in atmospheric oxygen correlated to the radiations of terrestrial plants and large predatory fish. *PNAS* 107, 17911–17915.
- Dellwig, O., Schnetger, B., Meyer, D., Pollehn, F., Hausler, K., Arz, H.W., 2018. Impact of the Major Baltic Inflow in 2014 on Manganese Cycling in the Gotland Deep (Baltic Sea). *Front. Mar. Sci.* 5, 20.
- Dickson, A.J., 2017. A molybdenum-isotope perspective on Phanerozoic deoxygenation events. *Nat. Geosci.* 10, 721–726.
- Dong, Z.G., Zhang, L.C., Dong, F.Y., Zhang, B.L., Xie, Y.Q., Zha, B., Peng, Z.D., Wang, C.L., 2020. Geological characteristics, ore-controlling factors and metallogenic model of Muhu manganese deposit in the West Kunlun, China. *J. Jilin Univ. (Earth Sci. Ed.)* 50, 1358–1372 (in Chinese with English Abstract).
- Dong, Z.G., Peng, Z.D., Wang, C.L., Zhang, B.L., Zhang, L.C., Li, J., Zhang, X., Li, W.J., Zhang, L., 2022. Insight into the genesis of the Zhaosu Carboniferous Mn carbonate deposit (NW China): constraints from petrography, geochemistry, and C-Mo isotopes. *Miner. Deposita* 57, 1269–1289.
- Emmings, J.F., Poulton, S.W., Vane, C.H., Davies, S.J., Jenkin, G.R.T., Stephenson, M.H., Leng, M.J., Lamb, A.L., Moss-Hayes, V., 2020. A Mississippian black shale record of redox oscillation in the Craven Basin, UK. *Palaeogeogr. Palaeoclimatol. Palaeoecol.* 538, 109423.
- Fan, D.L., Liu, T.B., Ye, J., 1992. The process of formation of manganese carbonate deposits hosted in black shale series. *Econ. Geol.* 87, 1419–1429.
- Force, E.R., Cannon, W.F., 1988. Depositional model for shallow marine manganese deposits around black shale basins. *Econ. Geol.* 83, 93–117.
- Frakes, L.A., Bolton, B.R., 1984. Origin of manganese giants: sea-level change and anoxic-oxic history. *Geology* 12, 83–86.

- Frakes, L.A., Bolton, B.R., 1992. Effects of ocean chemistry, sea-level, and climate on the formation of primary sedimentary manganese ore-deposits. *Econ. Geol.* 87, 1207–1217.
- Gao, Y.B., Teng, J.X., Li, W.Y., Chen, D.H., Sui, Q.L., Jing, D.L., He, Y.K., Bai, J.K., 2018. Geology, geochemistry and ore genesis of the Aoertuokanashi manganese deposit, western Kunlun, Xinjiang, Northwest China. *Acta Petrol. Sin.* 34, 2341–2358 (in Chinese with English abstract).
- Gaspers, N., Magna, T., Ackerman, L., 2020. Molybdenum Mass Fractions and Stable Isotope Compositions of Sedimentary Carbonate and Silicate Reference Materials. *Geostand. Geoanal. Res.* 44, 363–374.
- Gilleaudeau, G.J., Algeo, T.J., Lyons, T.W., Bates, S., Anbar, A.D., 2021. Novel watermass reconstruction in the Early Mississippian Appalachian Seaway based on integrated proxy records of redox and salinity. *Earth Planet. Sci. Lett.* 558, 116746.
- Goldberg, T., Archer, C., Vance, D., Poulton, S.W., 2009. Mo isotope fractionation during adsorption to Fe (oxyhydr)oxides. *Geochim. Cosmochim. Acta* 73, 6502–6516.
- Goto, K.T., Sekine, Y., Shimoda, G., Hein, J.R., Aoki, S., Ishikawa, A., Suzuki, K., Gordon, G.W., Anbar, A.D., 2020. A framework for understanding Mo isotope records of Archean and Paleoproterozoic Fe- and Mn-rich sedimentary rocks: Insights from modern marine hydrothermal Fe-Mn oxides. *Geochim. Cosmochim. Acta* 280, 221–236.
- Goto, K.T., Sekine, Y., Ito, T., Suzuki, K., Anbar, A.D., Gordon, G.W., Harigane, Y., Maruoka, T., Shimoda, G., Kashiwabara, T., Takaya, Y., Nozaki, T., Hein, J.R., Tetteh, G.M., Nyame, F.K., Kiyokawa, S., 2021. Progressive ocean oxygenation at ~2.2 Ga inferred from geochemistry and molybdenum isotopes of the Nsuta Mn deposit, Ghana. *Chemical Geology* 567, 120116.
- Grasby, S.E., Bond, D.P.G., Wignall, P.B., Yin, R., Strachan, L.J., Takahashi, S., 2021. Transient Permian-Triassic euxinia in the southern Panthalassa deep ocean. *Geology* 49, 889–893.
- Gutzmer, J., Beukes, N.J., 1998. The manganese formation of the Neoproterozoic Penganga Group, India - Revision of an enigma. *Econ. Geol.* 93, 1091–1102.
- Han, Y.G., Zhao, G.C., Cawood, P.A., Sun, M., Eizenhöfer, P.R., Hou, W.Z., Zhang, X.R., Liu, Q., 2016. Tarim and North China cratons linked to northern Gondwana through switching accretionary tectonics and collisional orogenesis. *Geology* 44, 95–98.
- Hardisty, D.S., Riedinger, N., Planavsky, N.J., Asael, D., Andren, T., Jorgensen, B.B., Lyons, T.W., 2016. A Holocene history of dynamic water column redox conditions in the Landsort deep, Baltic sea. *Am. J. Sci.* 316, 713–745.
- Häusler, K., Dellwig, O., Schnetger, B., Feldens, P., Leipe, T., Moros, M., Pollehn, F., Schonke, M., Wegwerth, A., Arz, H.W., 2018. Massive Mn carbonate formation in the Landsort Deep (Baltic Sea): Hydrographic conditions, temporal succession, and Mn budget calculations. *Mar. Geol.* 395, 260–270.
- Hein, J.R., Fan, D.L., Ye, J., Liu, T.B., Yeh, H.W., 1999. Composition and origin of Early Cambrian Tiantaishan phosphorite–Mn carbonate ores, Shaanxi Province, China. *Ore Geol. Rev.* 15, 95–134.
- Hein, J.R., Mizell, K., Koschinsky, A., Conrad, T.A., 2013. Deep-ocean mineral deposits as a source of critical metals for high- and green-technology applications: Comparison with land-based resources. *Ore Geol. Rev.* 51, 1–14.
- Helz, G.R., Bura-Nakic, E., Mikac, N., Ciglenecki, I., 2011. New model for molybdenum behavior in euxinic waters. *Chem. Geol.* 284, 323–332.
- Hem, J.D., 1972. Chemical factors that influence the availability of iron and manganese in aqueous systems. *Geol. Soc. Am. Bull.* 83, 443–450.
- Hermans, M., Lenstra, W.K., van Helmond, N., Behrends, T., Egger, M., Seguret, M.J.M., Gustafsson, E., Gustafsson, B.G., Slomp, C.P., 2019. Impact of natural re-oxygenation on the sediment dynamics of manganese, iron and phosphorus in a euxinic Baltic Sea basin. *Geochim. Cosmochim. Acta* 246, 174–196.
- Herndon, E.M., Havig, J.R., Singer, D.M., McCormick, M.L., Kump, L.R., 2018. Manganese and iron geochemistry in sediments underlying the redox-stratified Fayetteville Green Lake. *Geochim. Cosmochim. Acta* 231, 50–63.
- Huang, Q., Pi, D.H., Jiang, S.Y., Liu, D., Yan, H., Mänd, K., Kirsimäe, K., Bishop, B., Robbins, L.J., Yang, S.S., 2022. The dual role of microbes in the formation of the Malkantu manganese carbonate deposit, NW China: Petrographic, geochemical, and experimental evidence. *Chem. Geol.* 606, 120992.
- Huckriede, H., Meischner, D., 1996. Origin and environment of manganese-rich sediments within black-shale basins. *Geochim. Cosmochim. Acta* 60, 1399–1413.
- Isbell, J.L., Henry, L.C., Gulbranson, E.L., Limarino, C.O., Fraiser, M.L., Koch, Z.J., Ciccio, P.L., Dineen, A.A., 2012. Glacial paradoxes during the late Paleozoic ice age: Evaluating the equilibrium line altitude as a control on glaciation. *Gondw. Res.* 22, 1–19.
- Jenkyns, H.C., Géczy, B., Marshall, J.D., 1991. Jurassic Manganese Carbonates of Central Europe and the Early Toarcian Anoxic Event. *J. Geol.* 99, 137–149.
- Ji, W.H., Chen, S.J., Li, R.S., He, S.P., Zhao, Z.M., Pan, X.P., 2018. The origin of Carboniferous-Permian magmatic rocks in Oytang area, West Kunlun: Back-arc basin? *Acta Petrol. Sin.* 34, 2393–2409 (In Chinese with English abstract).
- Johnson, J.E., Webb, S.M., Ma, C., Fischer, W.W., 2016. Manganese mineralogy and diagenesis in the sedimentary rock record. *Geochim. Cosmochim. Acta* 173, 210–231.
- Kendall, B., Dahl, T.W., Anbar, A.D., 2017. Good Golly, Why Moly? The stable isotope geochemistry of molybdenum. *Rev. Mineral. Geochem.* 82, 683–732.
- Kendall, B., Wang, J., Zheng, W., Romaniello, S.J., Over, D.J., Bennett, Y., Xing, L., Kunert, A., Boyes, C., Liu, J., 2020. Inverse correlation between the molybdenum and uranium isotope compositions of Upper Devonian black shales caused by changes in local depositional conditions rather than global ocean redox variations. *Geochim. Cosmochim. Acta* 287, 141–164.
- King, E.K., Perakis, S.S., Pett-Ridge, J.C., 2018. Molybdenum isotope fractionation during adsorption to organic matter. *Geochim. Cosmochim. Acta* 222, 584–598.
- Klinkhammer, G.P., Palmer, M.R., 1991. Uranium in the oceans: Where it goes and why. *Geochim. Cosmochim. Acta* 55, 1799–1806.
- Krauskopf, K.B., 1957. Separation of manganese from iron in sedimentary processes. *Geochim. Cosmochim. Acta* 12, 61–84.
- Lenstra, W.K., Séguret, M.J.M., Behrends, T., Groeneveld, R.K., Hermans, M., Witbaard, R., Slomp, C.P., 2020. Controls on the shuttling of manganese over the northwestern Black Sea shelf and its fate in the euxinic deep basin. *Geochim. Cosmochim. Acta* 273, 177–204.
- Lepland, A., Stevens, R.L., 1998. Manganese authigenesis in the Landsort Deep, Baltic Sea. *Mar. Geol.* 151, 1–25.
- Li, W.Y., 2018. The primary discussion on the relationship between Paleo-Asian Ocean and Paleo-Tethys Ocean. *Acta Petrol. Sin.* 34, 2201–2210 (in Chinese with English abstract).
- Li, J., Liang, X.R., Zhong, L.F., Wang, X.C., Ren, Z.Y., Sun, S.L., Zhang, Z.F., Xu, J.F., 2014. Measurement of the isotopic composition of Molybdenum in geological samples by MC-ICP-MS using a novel chromatographic extraction technique. *Geostand. Geoanal. Res.* 38, 345–354.
- Li, W.J., Peng, Z.D., Dong, Z.G., Zhang, B.L., Gao, B.Y., Zhang, L.C., Zhu, M.T., Robbins, L.J., Konhauser, K.O., 2022. Direct Re-Os Dating Of Manganese Carbonate Ores And Implications For The Formation Of The Ortokarnash Manganese Deposit, Northwest China. *Econ. Geol.* 117, 237–252.
- Little, S.H., Vance, D., Lyons, T.W., McManus, J., 2015. Controls on trace metal authigenic enrichment in reducing sediments: insights from modern oxygen-deficient settings. *Am. J. Sci.* 315, 77–119.
- Liu, T.B., 1990. C-S-Fe relationships in shales hosting manganese ores from Mexico, China, and Newfoundland: Implications for depositional environment and mineralization. *Ore Geol. Rev.* 5, 325–340.
- Lu, X.Z., Dahl, T.W., Zheng, W., Wang, S., Kendall, B., 2020. Estimating ancient seawater isotope compositions and global ocean redox conditions by coupling the molybdenum and uranium isotope systems of euxinic organic-rich mudrocks. *Geochim. Cosmochim. Acta* 290, 76–103.
- Lyons, T.W., Diamond, C.W., Konhauser, K.O., 2020. Shedding light on manganese cycling in the early oceans. In: *Proceedings of the National Academy of Sciences of the United States of America* 117, 25960–25962.
- Mänd, K., Lalonde, S.V., Robbins, L.J., Thoby, M., Paiste, K., Kreitsmann, T., Paiste, P., Reinhard, C.T., Romashkin, A.E., Planavsky, N.J., Kirsimäe, K., Lepland, A., Konhauser, K.O., 2020. Palaeoproterozoic oxygenated oceans following the Lomagundi-Jatuli Event. *Nat. Geosci.*
- März, C., Poulton, S.W., Beckmann, B., Küster, K., Wagner, T., Kasten, S., 2008. Redox sensitivity of P cycling during marine black shale formation: dynamics of sulfidic and anoxic, non-sulfidic bottom waters. *Geochim. Cosmochim. Acta* 72, 3703–3717.
- Mattern, F., Schneider, W., 2000. Suturing of the Proto- and Paleo-Tethys oceans in the western Kunlun (Xinjiang, China). *J. Asian Earth Sci.* 18, 637–650.
- Maynard, J.B., 2010. The chemistry of manganese ores through time: A signal of increasing diversity of Earth-surface environments. *Econ. Geol.* 105, 535–552.
- McManus, J., Nagler, T.F., Siebert, C., Wheat, C.G., Hammond, D.E., 2002. Oceanic molybdenum isotope fractionation: Diagenesis and hydrothermal ridge-flank alteration. *Geochim. Cosmochim. Acta* 66, 1–9.
- Meischner, D. (1971) Clastic sedimentation in the Variscan geosyncline east of the river Rhine. In: Müller, G. (Eds.) *Sedimentary of parts of Central Europe, Guidebook*, pp. 9–43. VIII International Sedimentology Congress. 1971, Heidelberg.
- Nägler, T.F., Neubert, N., Böttcher, M.E., Dellwig, O., Schnetger, B., 2011. Molybdenum isotope fractionation in pelagic euxinia: evidence from the modern Black and Baltic Seas. *Chem. Geol.* 289, 1–11.
- Nägler, T.F., Anbar, A.D., Archer, C., Goldberg, T., Gordon, G.W., Greber, N.D., Siebert, C., Sohrin, Y., Vance, D., 2014. Proposal for an international Molybdenum isotope measurement standard and data representation. *Geostand. Geoanal. Res.* 38, 149–151.
- Neubert, N., Nagler, T.F., Böttcher, M.E., 2008. Sulfidity controls molybdenum isotope fractionation into euxinic sediments: Evidence from the modern Black Sea. *Geology* 36, 775–778.
- Noordmann, J., Weyer, S., Montoya-Pino, C., Dellwig, O., Neubert, N., Eckert, S., Paetzel, M., Böttcher, M.E., 2015. Uranium and molybdenum isotope systematics in modern euxinic basins: Case studies from the central Baltic Sea and the Kyllaren fjord (Norway). *Chem. Geol.* 396, 182–195.
- Nozaki, Y., Zhang, J., Amakawa, H., 1997. The fractionation between Y and Ho in the marine environment. *Earth Planet. Sci. Lett.* 148, 329–340.
- Okita, P.M., 1992. Manganese carbonate mineralization in the Molango District, Mexico. *Econ. Geol.* 87, 1345–1366.
- Okita, P.M., Shanks, W.C., 1992. Origin of stratiform sediment-hosted manganese carbonate ore deposits: Examples from Molango, Mexico, and Taoliang, China. *Chem. Geol.* 99, 139–163.
- Okita, P.M., Maynard, J.B., Spiker, E.C., Force, E.R., 1988. Isotopic evidence for organic matter oxidation by manganese reduction in the formation of stratiform manganese carbonate ore. *Geochim. Cosmochim. Acta* 52, 2679–2685.
- Ossa, O.F., Hofmann, A., Wille, M., Spangenberg, J.E., Bekker, A., Poulton, S.W., Eickmann, B., Schoenberg, R., 2018. Aerobic iron and manganese cycling in a redox-stratified Mesoproterozoic epicontinental sea. *Earth Planet. Sci. Lett.* 500, 28–40.
- Ostrander, C.M., Sahoo, S.K., Kendall, B., Jiang, G.Q., Planavsky, N.J., Lyons, T.W., Nielsen, S.G., Owens, J.D., Gordon, G.W., Romaniello, S.J., Anbar, A.D., 2019. Multiple negative molybdenum isotope excursions in the Doushantuo

- Formation (South China) fingerprint complex redox-related processes in the Ediacaran Nanhua Basin. *Geochim. Cosmochim. Acta* 261, 191–209.
- Peers, G., Price, N.M., 2004. A role for manganese in superoxide dismutases and growth of iron-deficient diatoms. *Limnol. Oceanogr.* 49, 1774–1783.
- Peng, J.W., Fu, Q.L., Larson, T.E., Janson, X., 2021a. Trace-elemental and petrographic constraints on the severity of hydrographic restriction in the silled Midland Basin during the late Paleozoic ice age. *Geol. Soc. Am. Bull.* 133, 57–73.
- Peng, Z.D., Zheng, M.T., Wang, C.L., Zhang, L.C., Fan, L.G., Tong, X.X., 2021b. Constraints on the age and geodynamic setting of the iron formations and anhydrite Fe-(Ba) deposits in the Bulunkuoale Group of the Taxkorgan area, NW China. *Ore Geology Reviews* 133, 104121.
- Planavsky, N.J., Dan, A., Hofmann, A., Reinhard, C.T., Lalonde, S.V., Knudsen, A., Wang, X., Ossa, O.F., Pecoits, E., Smith, A.J.B., 2014. Evidence for oxygenic photosynthesis half a billion years before the Great Oxidation Event. *Nat. Geosci.* 7, 283–286.
- Planavsky, N.J., Slack, J.F., Cannon, W.F., O'Connell, B., Isson, T.T., Asael, D., Jackson, J. C., Hardisty, D.S., Lyons, T.W., Bekker, A., 2018. Evidence for episodic oxygenation in a weakly redox-buffered deep mid-Proterozoic ocean. *Chem. Geol.* 483, 581–594.
- Planavsky, N.J., Robbins, L.J., Kamber, B.S., Schoenberg, R., 2020. Weathering, alteration and reconstructing Earth's oxygenation. *Interface Focus* 10, 10.
- Polgári, M., Okita, P.M., Hein, J.R., 1991. Stable isotope evidence for the origin of the Úrkút manganese ore deposit, Hungary. *J. Sediment. Petrol.* 61, 384–393.
- Polgári, M., Hein, J.R., Bíró, L., Gyollai, L., Németh, T., Sajgó, C., Fekete, J., Schwark, L., Pál-Molnár, E., Hámor-Vidó, M., Vigh, T., 2016. Mineral and chemostratigraphy of a Toarcian black shale hosting Mn-carbonate microbialites (Úrkút, Hungary). *Palaeogeogr. Palaeoclimatol. Palaeoecol.* 459, 99–120.
- Post J.E., 1999. Manganese oxide minerals: Crystal structures and economic and environmental significance. In: *Proceedings of the National Academy of Sciences of the United States of America* 96, 3447–3454.
- Poulton, S.W., Canfield, D.E., 2005. Development of a sequential extraction procedure for iron: implications for iron partitioning in continentally derived particulates. *Chem. Geol.* 214, 209–221.
- Poulton, S.W., Canfield, D.E., 2011. Ferruginous conditions: A dominant feature of the ocean through Earth's history. *Elements* 7, 107–112.
- Raiswell, R., Hardisty, D.S., Lyons, T.W., Canfield, D.E., Owens, J.D., Planavsky, N.J., Poulton, S.W., Reinhard, C.T., 2018. The Iron Paleoredox Proxies: A Guide To The Pitfalls, Problems And Proper Practice. *Am. J. Sci.* 318, 491–526.
- Robertson, A.H.F., Necdet, M., Raffi, I., Chen, G.H., 2019. Early Messinian manganese deposition in NE Cyprus related to cyclical redox changes in a silled hemipelagic basin prior to the Mediterranean salinity crisis. *Sed. Geol.* 385, 126–148.
- Roy, S., 2006. Sedimentary manganese metallogenesis in response to the evolution of the Earth system. *Earth Sci. Rev.* 77, 273–305.
- Schmidt, M., Botz, R., Faber, E., Schmitt, M., Poggenburg, J., Garbe-Schönberg, D., Stoffers, P., 2003. High-resolution methane profiles across anoxic brine-seawater boundaries in the Atlantis-II, Discovery, and Kebrit Deep (Red Sea). *Chem. Geol.* 200, 359–375.
- Scholz, F., McManus, J., Sommer, S., 2013. The manganese and iron shuttle in a modern euxinic basin and implications for molybdenum cycling at euxinic ocean margins. *Chem. Geol.* 355, 56–68.
- Scott, C., Lyons, T.W., 2012. Contrasting molybdenum cycling and isotopic properties in euxinic versus non-euxinic sediments and sedimentary rocks: Refining the paleoproxies. *Chem. Geol.* 324–325, 19–27.
- Shen, J., Feng, Q.L., Algeo, T.J., Li, C., Planavsky, N.J., Zhou, L., Zhang, M.L., 2016. Two pulses of oceanic environmental disturbance during the Permian-Triassic boundary crisis. *Earth Planet. Sci. Lett.* 443, 139–152.
- Shields, G., Stille, P., 2001. Diagenetic constraints on the use of cerium anomalies as palaeoseawater redox proxies: an isotopic and REE study of Cambrian phosphorites. *Chem. Geol.* 175, 29–48.
- Steiner, M., Wallis, E., Erdtmann, B.-D., Zhao, Y., Yang, R., 2001. Submarine-hydrothermal exhalative ore layers in black shales from South China and associated fossils – insights into a Lower Cambrian facies and bio-evolution. *Palaeogeogr. Palaeoclimatol. Palaeoecol.* 169, 165–191.
- Taylor, S.R., McLennan, S.M., 1985. The continental crust: its composition and evolution. Blackwell Scientific Publications, Oxford.
- Tebo, B.M., Bargar, J.R., Clement, B.G., Dick, G.J., Murray, K.J., Parker, D., Verity, R., Webb, S.M., 2004. Biogenic manganese oxides: Properties and mechanisms of formation. *Annu. Rev. Earth Planet. Sci.* 32, 287–328.
- Tossell, J.A., 2005. Calculating the partitioning of the isotopes of Mo between oxidic and sulfidic species in aqueous solution. *Geochim. Cosmochim. Acta* 69, 2981–2993.
- Tostevin, R., Wood, R.A., Shields, G.A., Poulton, S.W., Guilbaud, R., Bowyer, F., Penny, A.M., He, T., Curtis, A., Hoffmann, K.H., Clark, M.O., 2016. Low-oxygen waters limited habitable space for early animals. *Nat. Commun.* 7, 1–9.
- Tribouillard, N., Algeo, T.J., Lyons, T., Riboulleau, A., 2006. Trace metals as paleoredox and paleoproductivity proxies: An update. *Chem. Geol.* 232, 12–32.
- Tribouillard, N., Algeo, T.J., Baudin, F., Riboulleau, A., 2012. Analysis of marine environmental conditions based on molybdenum–uranium covariation—Applications to Mesozoic paleoceanography. *Chem. Geol.* 324–325, 46–58.
- Tsikos, H., Beukes, N.J., Moore, J.M., Harris, C., 2003. Deposition, diagenesis, and secondary enrichment of metals in the Paleoproterozoic Hotazel iron Formation, Kalahari manganese field, South Africa. *Econ. Geol.* 98, 1449–1462.
- Von Damm, K.L., Edmond, J.M., Measures, C.I., Grant, B., 1985. Chemistry of submarine hydrothermal solutions at Guaymas Basin, Gulf of California. *Geochim. Cosmochim. Acta* 49, 2221–2237.
- Wasylenki, L.E., Rolfe, B.A., Weeks, C.L., Spiro, T.G., Anbar, A.D., 2008. Experimental investigation of the effects of temperature and ionic strength on Mo isotope fractionation during adsorption to manganese oxides. *Geochim. Cosmochim. Acta* 72, 5997–6005.
- Wasylenki, L.E., Weeks, C.L., Bargar, J.R., Spiro, T.G., Hein, J.R., Anbar, A.D., 2011. The molecular mechanism of Mo isotope fractionation during adsorption to birnessite. *Geochim. Cosmochim. Acta* 75, 5019–5031.
- Wilkin, R.T., Barnes, H.L., Brantley, S.L., 1996. The size distribution of framboidal pyrite in modern sediments: An indicator of redox conditions. *Geochim. Cosmochim. Acta* 60, 3897–3912.
- Wilkin, R.T., Arthur, M.A., Dean, W.E., 1997. History of water-column anoxia in the Black Sea indicated by pyrite framboid size distributions. *Earth Planet. Sci. Lett.* 148, 517–525.
- Wittkop, C., Swanner, E.D., Grengs, A., Lambrecht, N., Fakhraee, M., Myrbo, A., Bray, A.W., Poulton, S.W., Katsev, S., 2020. Evaluating a primary carbonate pathway for manganese enrichments in reducing environments. *Earth Planet. Sci. Lett.* 538, 116–201.
- Wu, H.P., Jiang, S.Y., Palmer, M.R., Wei, H.Z., Yang, J.H., 2019. Positive cerium anomaly in the Doushantuo cap carbonates from the Yangtze platform, South China: Implications for intermediate water column manganese conditions in the aftermath of the Marinoan glaciation. *Precamb. Res.* 320, 93–110.
- Xiao, W.J., Han, F.L., Windley, B.F., Yuan, C., Zhou, H., Li, J.L., 2003. Multiple Accretionary Orogenesis and Episodic Growth of Continents: Insights from the Western Kunlun Range, Central Asia. *Int. Geol. Rev.* 45, 303–328.
- Xiao, J.F., He, J.Y., Yang, H.Y., Wu, C.Q., 2017. Comparison between Datangpo-type manganese ores and modern marine ferromanganese oxyhydroxide precipitates based on rare earth elements. *Ore Geol. Rev.* 89, 290–308.
- Xiao, W.J., Windley, B.F., Liu, D.Y., Jian, P., Liu, C.Z., Yuan, C., Sun, M., 2005. Accretionary tectonics of the Western Kunlun Orogen, China: A Paleozoic–early Mesozoic, long-lived active continental margin with implications for the growth of southern Eurasia. *J. Geol.* 113, 687–705.
- Xie, X.M., Zhu, G.Y., Wang, Y., 2021. The influence of syngenetic hydrothermal silica fluid on organic matter preservation in lower Cambrian Niutitang Formation. *South China. Mar. Pet. Geol.* 129, 105098.
- Xu, L.G., Frank, A.B., Lehmann, B., Zhu, J.M., Mao, J.W., Ju, Y.Z., Frei, R., 2019. Subtle Cr isotope signals track the variably anoxic Cryogenian interglacial period with voluminous manganese accumulation and decrease in biodiversity. *Sci Rep* 9, 8.
- Yan, H., Pi, D.H., Jiang, S.Y., Hao, W.D., Cui, H., Robbins, L.J., Mänd, K., Li, L., Planavsky, N.J., Konhauser, K.O., 2020. Hydrothermally induced ³⁴S enrichment in pyrite as an alternative explanation of the Late-Devonian sulfur isotope excursion in South China. *Geochim. Cosmochim. Acta* 283, 1–21.
- Yan, H., Pi, D.H., Jiang, S.Y., Mao, J.W., Xu, L.G., Yang, X.Q., Hao, W.D., Mänd, K., Li, L., Konhauser, K.O., Robbins, L.J., 2022. Mineral paragenesis in Paleozoic manganese ore deposits: Depositional versus post-depositional formation processes. *Geochim. Cosmochim. Acta* 325, 65–86.
- Yu, W.C., Algeo, T.J., Du, Y.S., Maynard, B., Guo, H., Zhou, Q., Peng, T.P., Wang, P., Yuan, L.J., 2016. Genesis of Cryogenian Datangpo manganese deposit: Hydrothermal influence and episodic post-glacial ventilation of Nanhua Basin, South China. *Palaeogeogr. Palaeoclimatol. Palaeoecol.* 459, 321–337.
- Yun, J., Gao, X.F., Xiao, P.X., Kang, L., Li, P., 2015. Geochemical characteristics of the Lower Carboniferous volcanic rocks of the Wuluat Formation in the Western Kunlun Mountains and their geological significance. *Geology of China* 42, 587–600 (in Chinese with English abstract).
- Zhang, B.L., 2020. Depositional environment and mineralization mechanism of the giant Ortokarnash manganese carbonate deposit in the Western Kunlun Mountains. PhD University of Chinese Academy of Sciences (In Chinese with English abstract).
- Zhang, B.L., Wang, C.L., Robbins, L.J., Zhang, L.C., Konhauser, K.O., Dong, Z.G., Li, W.J., Peng, Z.D., Zheng, M.T., 2020a. Petrography and Geochemistry of the Carboniferous Ortokarnash Manganese Deposit in the Western Kunlun Mountains, Xinjiang Province, China: Implications for the Depositional Environment and the Origin of Mineralization. *Econ. Geol.* 115, 1559–1588.
- Zhang, B.L., Lv, Z.C., Dong, Z.G., Zhang, X., Yu, X.F., Li, Y.S., Zhen, S.M., Wang, C.L., 2022. Source Characteristics of the Carboniferous Ortokarnash Manganese Deposit in the Western Kunlun Mountains. *Minerals* 12, 1–24.
- Zhang, K., Shields, G.A., 2022. Sedimentary Ce anomalies: Secular change and implications for paleoenvironmental evolution. *Earth Sci. Rev.* 229, 104015.
- Zhang, Z.W., Yang, X.Y., Zhang, L.C., Wu, C.Q., Luo, T.Y., Zhu, W.G., Xu, J.H., Hu, P.C., Li, X.Y., Jin, Z.R., 2021. Sedimentation and mineralization of the Late Paleozoic extensional basin in the western Kunlun Mountains, China. *Solid Earth Sciences* 6, 142–177.
- Zhang, L.C., Zhang, B.L., Dong, Z.G., Xie, Y.Q., Li, W.J., Peng, Z.D., Zhu, M.T., Wang, C.L., 2020b. Tectonic setting and metallogenetic conditions of the Carboniferous Malkansu giant manganese belt in the West Kunlun Orogen. *J. Jilin Univ. (Earth Sci. Ed.)* 50, 1340–1357 (In Chinese with English abstract).
- Zhang, C.L., Zou, H.B., Ye, X.T., Chen, X.Y., 2018. Timing of subduction initiation in the Proto-Tethys Ocean: Evidence from the Cambrian gabbros from the NE Pamir Plateau. *Lithos* 314–315, 40–51.
- Zhang, C.L., Zou, H.B., Ye, X.T., Chen, X.Y., 2019. Tectonic evolution of the West Kunlun Orogenic Belt along the northern margin of the Tibetan Plateau:

- Implications for the assembly of the Tarim terrane to Gondwana. *Geosci. Front.* 10, 973–988.
- Zhao, P.P., Li, J., Zhang, L., Wang, Z.B., Kong, D.X., Ma, J.L., Wei, G.J., Xu, J.F., 2016. Molybdenum mass fractions and isotopic compositions of international geological reference materials. *Geostand. Geoanal. Res.* 40, 217–226.
- Zheng, Y., Anderson, R.F., van Geen, A., Fleisher, M.Q., 2002. Preservation of particulate non-lithogenic uranium in marine sediments. *Geochim. Cosmochim. Acta* 66, 3085–3092.
- Zhou, X.Q., Chen, D.Z., Qing, H.R., Qian, Y.X., Wang, D., 2014. Submarine silica-rich hydrothermal activity during the earliest Cambrian in the Tarim Basin, Northwest China. *Int. Geol. Rev.* 56, 1906–1918.
- Zhou, Q., Du, Y.S., Yuan, L.J., Zhang, S., Yu, W.C., Yang, S.T., Liu, Y., 2016. The structure of the Wuling rift basin and its control on the manganese deposits during the Nanhua period in Guizhou–Hunan–Chongqing border area, South China. *Earth Sci.* 41, 177–188 (In Chinese with English abstract).